Laboratory study of low-β forces in arched, line-tied magnetic flux ropes

C. E. Myers,[1,2,a),b)] M. Yamada,[2] H. Ji,[1,2,3] J. Yoo,[2] J. Jara-Almonte,[1,2] and W. Fox[2]
[1]*Department of Astrophysical Sciences, Princeton University, Princeton, New Jersey 08544, USA*
[2]*Princeton Plasma Physics Laboratory, Princeton, New Jersey 08543, USA*
[3]*Laboratory for Space Environment and Physical Sciences, Harbin Institute of Technology, Harbin, Heilongjiang 150001, China*

(Received 2 July 2016; accepted 18 October 2016; published online 4 November 2016)

The loss-of-equilibrium is a solar eruption mechanism whereby a sudden breakdown of the magnetohydrodynamic force balance in the Sun's corona ejects a massive burst of particles and energy into the heliosphere. Predicting a loss-of-equilibrium, which has more recently been formulated as the torus instability, relies on a detailed understanding of the various forces that hold the pre-eruption magnetic flux rope in equilibrium. Traditionally, idealized analytical force expressions are used to derive simplified eruption criteria that can be compared to solar observations and modeling. What is missing, however, is a validation that these idealized analytical force expressions can be applied to the line-tied, low-aspect-ratio conditions of the corona. In this paper, we address this shortcoming by using a laboratory experiment to study the forces that act on long-lived, arched, line-tied magnetic flux ropes. Three key force terms are evaluated over a wide range of experimental conditions: (1) the upward hoop force; (2) the downward strapping force; and (3) the downward toroidal field tension force. First, the laboratory force measurements show that, on average, the three aforementioned force terms cancel to produce a balanced line-tied equilibrium. This finding validates the laboratory force measurement techniques developed here, which were recently used to identify a dynamic toroidal field tension force that can prevent flux rope eruptions [Myers *et al.*, Nature **528**, 526 (2015)]. The verification of magnetic force balance also confirms the low-β assumption that the plasma thermal pressure is negligible in these experiments. Next, the measured force terms are directly compared to corresponding analytical expressions. While the measured and analytical forces are found to be well correlated, the low-aspect-ratio, line-tied conditions in the experiment are found to both reduce the measured hoop force and increase the measured tension force with respect to analytical expectations. These two co-directed effects combine to generate laboratory flux rope equilibria at lower altitudes than are predicted analytically. Such considerations are expected to modify the loss-of-equilibrium eruption criteria for analogous flux ropes in the solar corona. *Published by AIP Publishing.*
[http://dx.doi.org/10.1063/1.4966691]

I. INTRODUCTION

The arched, line-tied magnetic flux rope is a magnetohydrodynamic structure that plays a key role in solar eruptive events such as solar flares and coronal mass ejections.[1,2] The prototypical flux rope is an arched tube of helical magnetic field lines and confined plasma whose footpoints are line-tied, or magnetically anchored, to the solar surface.[3–6] This footpoint line-tying breaks the flux rope's toroidal symmetry and changes both its equilibrium and its stability. Line-tied flux ropes are a central component of the "storage-and-release" paradigm for solar eruptions. Under this paradigm, the flux rope first stores magnetic energy in a quasi-statically evolving equilibrium before suddenly and dynamically releasing the stored energy during an eruption.[7,8] Consequently, understanding the physics that governs both the equilibrium and the stability of line-tied flux ropes is a key to predicting solar eruptions. In this paper, we introduce a laboratory experiment that is specifically designed to study storage-and-release phenomena in line-tied magnetic flux ropes.

One physical mechanism that can trigger storage-and-release eruptions is a loss-of-equilibrium, which occurs when the vertical force balance of a quasi-statically evolving flux rope breaks down suddenly and irreversibly. Originally formulated as a catastrophe mechanism,[9] the loss-of-equilibrium has more recently been studied in the context of an ideal magnetohydrodynamic instability called the torus instability.[10–14] The basic idea is that an upward perturbation of the flux rope will be unstable if the downward restraining forces acting on the rope decay more quickly with height than do the upward driving forces. For the torus instability, the restraining forces are assumed to be generated primarily by the interaction between the flux rope and an ambient "strapping" magnetic field. Thus, if this strapping field decays too quickly with height, then its associated restoring force is too weak to prevent the flux rope from erupting.[10,15]

The analytical loss-of-equilibrium criterion can be expressed concisely in terms of the vertical force per unit length F acting on the apex of the arched flux rope (i.e., at the top of the loop)

Paper YI3 1, Bull. Am. Phys. Soc. **60**, 392 (2015).
[a)]Invited speaker.
[b)]Electronic mail: cmyers@pppl.gov

$$\left.\frac{\partial F}{\partial z}\right|_{F=0} > 0, \tag{1}$$

where z is the vertical coordinate. This condition says that the equilibrium will be lost when the flux rope, upon being perturbed vertically upward from its equilibrium ($F = 0$) position, feels a positive (upward) force that reinforces the perturbation. The evaluation of the loss-of-equilibrium condition requires knowledge of both the equilibrium force balance and the response of the equilibrium forces to a dynamic upward perturbation. These two considerations can be separated as

$$\sum_i F_i = 0 \quad \text{and} \quad \sum_i \frac{\partial F_i}{\partial z} > 0, \tag{2}$$

where F_i is the individual force term contributing to the equilibrium. Thus, the key to understanding when a loss-of-equilibrium will be triggered lies in understanding the individual vertical forces acting on the arched magnetic flux rope.

In general, the magnetohydrodynamic forces acting on a line-tied flux rope are comprised of both Lorentz ($\mathbf{J} \times \mathbf{B}$) and thermal pressure ($\nabla p$) contributions. Fortunately, the conditions in the solar corona permit the elimination of the pressure gradient terms. More specifically, the corona is inherently low-β such that the magnetic pressure dominates the thermal pressure[16] and only the Lorentz forces need to be considered. Three key Lorentz force terms are considered in this paper: (1) the upward hoop force; (2) the downward strapping force; and (3) the downward toroidal field tension force. The traditional approach to treating these forces is to derive analytical expressions that can be used to evaluate the loss-of-equilibrium criterion in Eq. (1). The resulting stability criterion is then compared to solar observations and modeling in order to determine if a loss-of-equilibrium could have caused a given solar eruptive event. What is missing in this approach, however, is a validation of the analytical force expressions that are used to derive the loss-of-equilibrium criteria. Since these force expressions require assumptions and simplifications in order to be analytically tractable, there is no guarantee that they apply to the non-ideal, line-tied, low-aspect-ratio conditions of the solar corona. Thus, in this paper, we introduce a new tool for validating the analytical force expressions: the direct measurement of magnetohydrodynamic forces in a laboratory magnetic flux rope experiment.

The laboratory experiments introduced here are line-tied flux rope experiments wherein the arched flux rope plasma evolves quasi-statically so that storage-and-release phenomena can be studied in detail.[17] As such, these experiments are the first to provide comprehensive measurements of the magnetohydrodynamic forces that govern arched, line-tied flux ropes. This experimental capability has already been used to identify a new flux rope stability regime where a dynamic toroidal field tension force prevents otherwise torus-unstable flux ropes from erupting.[18] The present paper provides a full description of the experimental techniques that were developed to measure this toroidal field tension force. It also expands the force analysis to include a broad study of quasi-steady hoop, strapping, and tension forces across an ensemble of line-tied flux rope equilibria. Finally, it compares the experimentally measured forces directly to the analytical force expressions that are used to derive the torus instability criterion.[10,13,19]

The paper is organized as follows: First, Section II describes the various magnetic field, current density, and flux rope force terms that are treated in this paper. Analytical force expressions are derived that include compensations for the line-tied geometry of the flux rope, and the theoretical foundations for the torus and kink magnetohydrodynamic instabilities are reviewed. Section III introduces the laboratory flux rope experiments, which are conducted in the Magnetic Reconnection Experiment (MRX), and summarizes the key results that motivate the detailed study of flux rope forces presented here. Then, Section IV details the direct laboratory measurements of the various flux rope forces. Finally, Section V presents a comparison of experimentally measured forces to analytical expressions. This serves to validate some analytical force expressions and to highlight the shortcomings of others. A summary and discussion are presented in Section VI.

II. MAGNETIC FLUX ROPE FIELDS, FORCES, AND INSTABILITIES

In order to study the equilibrium and stability of line-tied magnetic flux ropes, it is necessary to identify the key components of the magnetic field $\mathbf{B}$ and the electric current $\mathbf{J}$ that make up the flux rope configuration. The various fields and currents interact to produce Lorentz forces that contribute to the flux rope equilibrium and stability. In this section, we derive various analytical Lorentz force expressions, some of which include corrections for the line-tied shape of the flux rope. These expressions are key to understanding the torus instability as a loss-of-equilibrium mechanism. They will be directly compared to the experimentally measured forces in Section V. We begin by describing the specific magnetic field and electric current decomposition used in this paper.

A. The magnetic field and electric current decomposition

As with any magnetized plasma, the magnetic fields in a line-tied flux rope can be separated into vacuum (external) and plasma (internal) components. The vacuum fields—also known as "potential" fields—are those that are generated by electric currents flowing outside of the flux rope plasma. In the corona, the vacuum fields are generated by external currents that flow across or beneath the solar photosphere. In the laboratory, such external currents instead flow in copper coils or in nearby conducting structures. In either case, the vacuum magnetic fields can be divided into two key components: (1) the guide field $\mathbf{B}_g$ which runs toroidally along the flux rope arch; and (2) the strapping field $\mathbf{B}_s$ which runs perpendicular to the flux rope arch (see Fig. 1). Each of these vacuum field components provides a restoring force that acts to confine the flux rope plasma in a quasi-statically evolving equilibrium.

In contrast to the vacuum magnetic fields, the plasma-generated fields are produced by currents flowing within the body of the flux rope plasma. It is the energy stored in these internal fields that drives the flux rope toward instability. Here, we choose to decompose the internal fields and currents

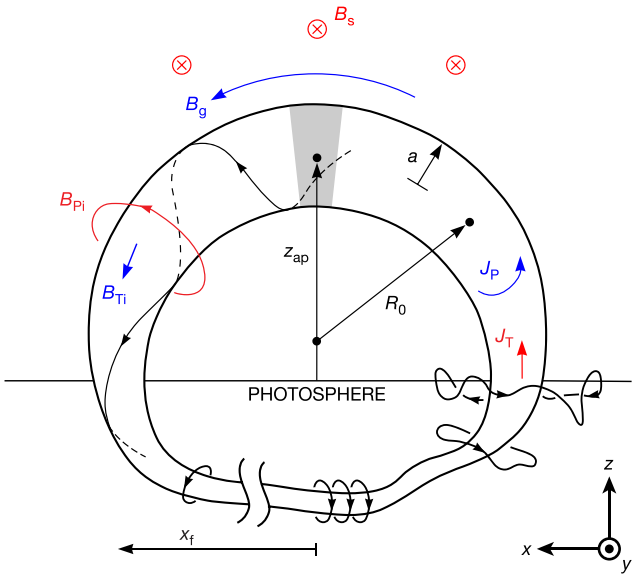

FIG. 1. Magnetic fields and currents in a line-tied magnetic flux rope. The arched flux rope is line-tied to the dense photosphere at two footpoints separated by $2x_f$. Those fields and currents associated with the poloidal magnetic field are shown in red, while those associated with the toroidal magnetic field are shown in blue. The forces described in this paper are evaluated at the flux rope apex, which is shaded in gray. Adapted with permission from Chen, Astrophys. J. **338**, 453 (1989) and Chen and Krall, J. Geophys. Res. Space **108**, 1410 (2003). Copyright 1989 American Astronomical Society and 2003 American Geophysical Union.[48]

into poloidal P and toroidal T components (see Fig. 1 and Table I). First, the toroidal flux rope current $\mathbf{J}_T$ generates an internal poloidal magnetic field $\mathbf{B}_{Pi}$. This internal poloidal field can be superposed with the external strapping field to compute the total poloidal field $\mathbf{B}_P = \mathbf{B}_s + \mathbf{B}_{Pi}$. Likewise, the poloidal flux rope current $\mathbf{J}_P$ generates an internal toroidal field $\mathbf{B}_{Ti}$ that can be superposed with $\mathbf{B}_g$ to compute the total toroidal field $\mathbf{B}_T = \mathbf{B}_g + \mathbf{B}_{Ti}$. With the various flux rope fields and currents in hand, we now derive expressions for the forces that these field and currents generate.

B. Analytical expressions for the flux rope forces

The magnetic field and electric current components introduced above interact to produce various $\mathbf{J} \times \mathbf{B}$ Lorentz forces that act on the body of the flux rope. We are interested, in particular, in the forces acting at the flux rope apex (i.e., the top of the loop) because this is the most likely trigger point for an eruption. Formally, the total vertical force per unit length F_z, acting at the flux rope apex ($z = z_{ap}$) can be defined as

$$F_z(z_{ap}) = \frac{1}{R_0\,\Delta T}\int_{-\Delta T/2}^{\Delta T/2} dT \int_0^{2\pi} d\theta \int_0^a dr\,\left[r\,h_T(z) f_z(r,\theta)\right], \quad (3)$$

where T is the toroidal coordinate, θ is the poloidal angle, and r is the minor radial coordinate. The integration is carried out over a wedge-shaped plasma volume with a major radius-of-curvature of R_0 and toroidal width ΔT. The poloidal boundary (i.e., the cross-section) of the wedge is defined by the minor radius $r = a(\theta)$. The utility of this formulation is that we can assume that locally $\partial/\partial T \simeq 0$ such that the above integral reduces to

$$F_z(z_{ap}) = \frac{1}{R_0}\int_0^{2\pi} d\theta \int_0^a dr\,\left[r\,h_T(z) f_z(r,\theta)\right]. \quad (4)$$

The quantity $h_T(z)$ in the integrand is the curvilinear scale factor that accounts for the out-of-plane toroidal curvature of the flux rope. In a Cartesian system $h_T = 1$, and in a cylindrical system $h_T = R$, but in general h_T is a non-trivial function of the height along the vertical axis.[20] Finally, the quantity $f_z(r,\theta)$ in the integrand is the volumetric $\mathbf{J} \times \mathbf{B}$ force density. Since we are only concerned in this paper with vertical (z-directed) forces, it is cumbersome to retain the subscript z in the force notation. We therefore adopt the convention that

$$f \equiv f_z = \hat{\mathbf{e}}_z \cdot \mathbf{f} \quad \text{and} \quad F \equiv F_z = \hat{\mathbf{e}}_z \cdot \mathbf{F}, \quad (5)$$

where the lowercase f represents a volumetric force density and the capital F represents a force per unit length.

The remaining task is to decompose the force density into various physically meaningful terms. The specific force decomposition used here considers three primary force terms: (1) the hoop force f_h; (2) the strapping force f_s; and (3) the toroidal field tension force f_t. In the coming subsections, we derive analytical expressions for the force per unit length generated at the apex of a line-tied flux rope by each of these Lorentz force terms. The various flux rope magnetic field, electric current, and Lorentz force terms are summarized in Table I.

TABLE I. Decomposition of the magnetic fields, electric currents, and Lorentz forces in a line-tied flux rope. Reprinted with permission from Myers *et al.*, Nature **528**, 526 (2015). Copyright 2015 Nature Publishing Group.

Quantity		Expression
Strapping field (vacuum)	$\mathbf{B}_s$	…
Internal poloidal field (flux rope)	$\mathbf{B}_{Pi}$	…
Guide field (vacuum)	$\mathbf{B}_g$	…
Internal toroidal field (flux rope)	$\mathbf{B}_{Ti}$	…
Total poloidal field	$\mathbf{B}_P$	$\mathbf{B}_s + \mathbf{B}_{Pi}$
Total toroidal field	$\mathbf{B}_T$	$\mathbf{B}_g + \mathbf{B}_{Ti}$
Toroidal current density	$\mathbf{J}_T$	$\nabla \times \mathbf{B}_{Pi}/\mu_0$
Poloidal current density	$\mathbf{J}_P$	$\nabla \times \mathbf{B}_{Ti}/\mu_0$
Hoop force density (upward)	f_h	$\hat{\mathbf{e}}_z \cdot (\mathbf{J}_T \times \mathbf{B}_{Pi})$
Strapping force density (downward)	f_s	$\hat{\mathbf{e}}_z \cdot (\mathbf{J}_T \times \mathbf{B}_s)$
Tension force density (downward)	f_t	$\hat{\mathbf{e}}_z \cdot (\mathbf{J}_P \times \mathbf{B}_T)$

1. The toroidally symmetric hoop force

The primary force that drives a line-tied flux rope to expand is the hoop force. This force, which is only present in a toroidally arched flux rope, is derived from a curvature-induced asymmetry in the poloidal magnetic field. In terms of $\mathbf{J} \times \mathbf{B}$ forces, the hoop force results from the interaction between the toroidal flux rope current density $\mathbf{J}_T$ and the self-generated internal poloidal magnetic field $\mathbf{B}_{Pi}$. The asymmetry in $\mathbf{B}_{Pi}$ appears because the various toroidal current segments that make up the rope produce a field that is stronger on the inboard side of the rope than on the outboard side. Thus, because the hoop force is generated primarily by

fields from non-local sources, the geometry of the flux rope must be accounted for in the calculation of the hoop force.

The canonical treatment of the hoop force considers a large aspect ratio, circular current loop of major radius R, and minor radius a. In this configuration, the hoop force is given by Shafranov[21] to be

$$F_h = \frac{\mu_0 I_T^2}{4\pi R}\left[\ln\left(\frac{8R}{a}\right) - 1 + \frac{\ell_i}{2}\right], \tag{6}$$

where I_T is the total toroidal flux rope current and ℓ_i is the normalized "internal inductance" that characterizes the distribution of toroidal current density within the cross-section of the rope. This quantity is calculated as $\ell_i \equiv \langle B_P^2\rangle / B_{Pa}^2$, where $B_{Pa} \equiv \mu_0 I_T / 2\pi a$ is the edge poloidal field and the quantity $\langle B_P^2\rangle$ is the cross-section average of B_P^2. Typical values for the internal inductance are $\ell_i = 0$ for a surface current distribution and $\ell_i = 0.5$ for a uniform current distribution. Equation (6) can quickly be derived from energy considerations using the expression for the self-inductance of a large aspect ratio circular current loop[21,22]

$$\mathcal{L} \simeq \mu_0 R\left[\ln\left(\frac{8R}{a}\right) - 2 + \frac{\ell_i}{2}\right] \equiv \mu_0 R\,\ell. \tag{7}$$

Here, we have defined the normalized inductance $\ell \equiv \ln(8R/a) - 2 + \ell_i/2$. The self-inductance $\mathcal{L}$ is related to the total magnetic energy of the system by $W_m = \frac{1}{2}\mathcal{L} I_T^2$, which, in turn, can be used to derive the hoop force per unit length

$$F_h = \frac{1}{2\pi R}\frac{\partial W_m}{\partial R} = \frac{I_T^2}{4\pi R}\frac{\partial \mathcal{L}}{\partial R} = \frac{\mu_0 I_T^2}{4\pi R}(\ell + 1). \tag{8}$$

This axisymmetric hoop force expression has been widely validated and implemented in the study of toroidally symmetric plasma configurations such as tokamaks (see, e.g., Wesson[23] and Miyamoto[24]). The line-tied flux ropes studied here, however, are neither axisymmetric nor large aspect ratio. We therefore now address the impact of the non-axisymmetric geometry of a line-tied flux rope on the hoop force.

2. The line-tied hoop force

When the flux rope is line-tied at two footpoints, the toroidal symmetry assumed in the above hoop force calculation is broken. This symmetry breaking has several important consequences, which include a modified toroidal current path, a modified toroidal curvature, and a toroidally varying minor radius. While the toroidal curvature and minor radius effects can be handled locally at the apex of the flux rope, the modified toroidal current path is a global effect that has profound consequences for the hoop force.

To approximate the toroidal current path in a line-tied flux rope, we introduce the "shifted-circle" model of Chen[4] (see Fig. 2). This model accounts for geometric features of the flux rope introduced by line-tying. In particular, the shifted-circle model defines the x-z trajectory of the flux rope magnetic axis in the region where $z > 0$. It asserts that the magnetic axis is a shifted circle that intersects the flux rope

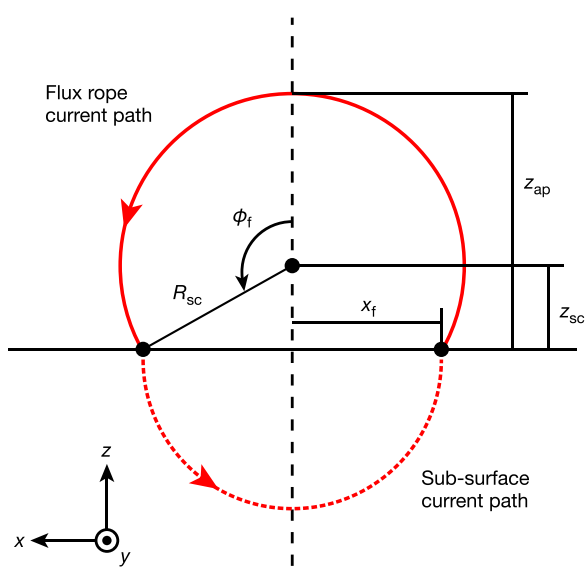

FIG. 2. Diagram of the magnetic axis profile for a line-tied flux rope. The shifted-circle model[4] is used for $z > 0$. The flux rope current path is a partial circle with a vertical radius-of-curvature R_{sc} and centroid height z_{sc} that are set so that the current path intersects the line-tied footpoints at $x = \pm x_f$ and reaches its apex at $z = z_{ap}$. In the case shown, the shifted-circle current path is closed beneath the $z = 0$ plane by a fixed semicircular current path. See the text for further discussion of relevant sub-surface current paths.

footpoints at $x = \pm x_f$ and reaches its apex at $z = z_{ap}$. The shifted circle's vertical radius-of-curvature R_{sc} and centroid height z_{sc} are therefore given by

$$R_{sc} = \frac{z_{ap}^2 + x_f^2}{2z_{ap}} \quad \text{and} \quad z_{sc} = \frac{z_{ap}^2 - x_f^2}{2z_{ap}}. \tag{9}$$

Note that these equations recover the circular profile of a toroidally symmetric ring when $z_{ap} = x_f$. For all z_{ap}, the angle ϕ_f from the z-axis to the footpoint at x_f is

$$\phi_f = \frac{\pi}{2} + \sin^{-1}\left(\frac{z_{sc}}{R_{sc}}\right), \tag{10}$$

such that the flux rope length is given by $L_{sc} = 2R_{sc}\phi_f$.

While the shifted-circle model defines the flux rope magnetic axis in the region where $z > 0$, it does not specify the sub-surface current path in the region where $z < 0$. There are several possible sub-surface current paths, the details of which vary with the system under consideration. Four sub-surface configurations of interest are shown in Fig. 3: (1) an axisymmetrically expanding loop; (2) the shifted-circle closure, which is assumed by Chen[4] and simply completes the $z > 0$ profile described by Eq. (9); (3) the image current closure, which assumes that the $z = 0$ plane is perfectly conducting such that the sub-surface current path is an image loop; and (4) the fixed current path closure, which is representative of the MRX laboratory flux rope experiments where the closure is completed by fixed copper cables. In the solar corona, on the other hand, where the photosphere acts as a highly conducting plane, the most relevant sub-surface closure is the image current case.[13,25]

With the shifted-circle model and the sub-surface configurations in hand, the remaining step is to investigate the impact of the line-tied toroidal current path on the hoop

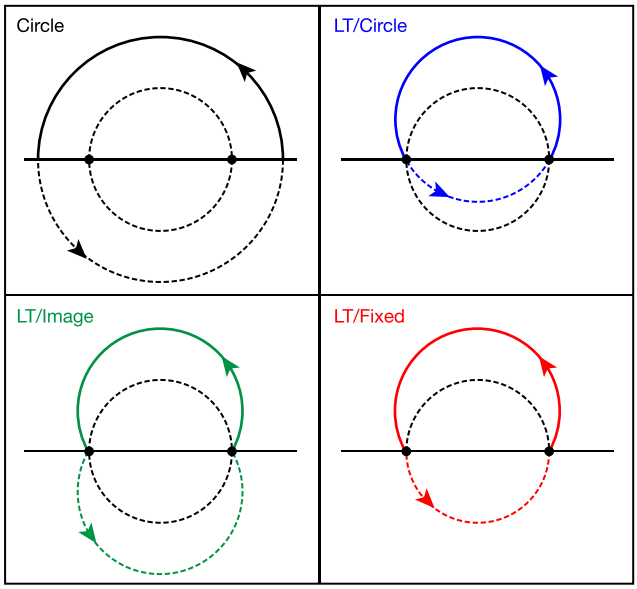

FIG. 3. Sub-surface closures for the line-tied (LT) flux rope: (a) axisymmetric flux rope for comparison to the various line-tied cases; (b) shifted circle closure (as assumed by Chen[4]); (c) image current closure, which approximates the solar case; (d) fixed current path closure, which approximates the laboratory case. The colored arrows indicate the direction of the current in each element of the current path.

force. This is achieved by inserting the shifted-circle major radius $R = R_{sc}(z)$ into the hoop force expression in Eq. (6). Additional corrections are introduced by accounting for the various sub-surface current paths introduced in Fig. 3. These corrections are numerically evaluated by computing the change in the internal poloidal field B_{Pi} at the flux rope apex that results from replacing the sub-surface shifted-circle current path with either the "image" current path or the "fixed" current path. The hoop force profiles that result from these various toroidal profile corrections are shown in Fig. 4, where the hoop force has been normalized to $F_{\text{norm}} \equiv \mu_0 I_T^2/4\pi x_f$. In the figure, we see that, in the region where $z_{ap}/x_f > 1$, the line-tied hoop forces (blue, green, red) behave similarly and decay more slowly than the axisymmetric hoop force (black). The behavior in the region where $z_{ap}/x_f < 1$, on the other hand, is highly dependent on the

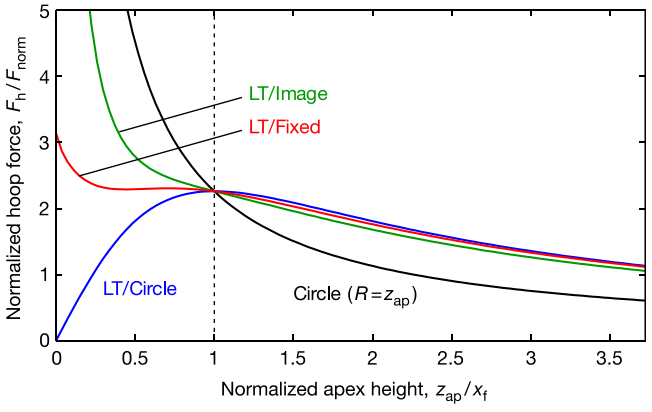

FIG. 4. Line-tied corrections to the hoop force. The forces are normalized to $F_{\text{norm}} \equiv \mu_0 I_T^2/4\pi x_f$, and the color coding of each hoop force profile is matched to the color coding in Fig. 3. Note that while the three line-tied (LT) profiles are similar for $z_{ap}/x_f > 1$, they differ substantially for $z_{ap}/x_f < 1$ where the details of the sub-surface closure become important.

structure of the current path that closes the loop beneath the $z = 0$ plane. In particular, the shifted-circle current path case limits to zero, the image current path case to infinity, and the fixed current path case to a finite value. As previously noted, the image profile is most applicable to the solar corona and the fixed profile is most applicable to the MRX experiments. The various sub-surface closures will be compared directly to experimentally measured hoop force data in Section V.

3. The poloidal field strapping force

The upwardly directed hoop force is opposed by the so-called strapping force, which serves to hold down the flux rope and prevent it from rising. In contrast to the hoop force, the strapping force is generated by the interaction between the plasma current and an externally generated poloidal magnetic field. In the solar case, this external field is derived from the potential magnetic field arcade within which the flux rope is embedded. In the laboratory case, this field is produced by purpose-built external magnetic field coils. Many treatments of solar flux ropes consider the strapping force to be the primary confining force in the system.[4,10,15] The volumetric strapping force is given by $f_s = \hat{\mathbf{e}}_z \cdot (\mathbf{J}_T \times \mathbf{B}_s)$. In general, this volumetric strapping force density must be integrated according to Eq. (3) to arrive at the strapping force per unit length F_s. In this case, however, we will approximate the flux rope as a line current, which simply gives

$$F_s \simeq -I_T B_{s0}, \tag{11}$$

where B_{s0} is the strapping field evaluated at the flux rope apex. Note that an explicit negative sign is included so that I_T and B_{s0} are positive-definite. As we will see, this simple form of the strapping force has surprising utility, even in cases where the flux rope is not well approximated as a thin line current.

4. The toroidal field tension force

Thus far, only forces from the poloidal magnetic field have been considered. As we will show, however, forces from the toroidal field are also important to the line-tied flux rope equilibrium. The vertical force density produced by the toroidal field is, in general, given by

$$f_t = \hat{\mathbf{e}}_z \cdot [\mathbf{J}_P \times \mathbf{B}_T] \quad \text{where} \quad \mathbf{J}_P = \frac{1}{\mu_0}\nabla \times \mathbf{B}_T. \tag{12}$$

The magnetic field can once again be separated into external and internal components, which for the toroidal field gives $B_T = B_g + B_{Ti}$. This decomposition recasts the above equations as

$$f_t = -J_P(B_g + B_{Ti}). \tag{13}$$

Unlike with the poloidal-field-generated force terms where the internal and external contributions are separated into the hoop and strapping forces, we elect here to retain a combined toroidal field tension force. Furthermore, we do not separate the toroidal field pressure and tension contributions such that the above equation for the toroidal field tension force includes both contributions. The next step is to analytically

evaluate the force per unit length acting on the flux rope due to the toroidal field tension force in Eq. (13).

a. The toroidal field tension force in the large aspect ratio limit. One of the key conclusions of this paper is that restraining forces from the toroidal magnetic field play a key role in the laboratory line-tied flux rope force balance. These restraining forces can be understood heuristically by considering a torus-shaped coil with helical windings (see Fig. 5). The toroidal curvature of the coil makes the density of windings (per unit length) higher on the inboard side of the coil than on the outboard side. If the toroidal magnetic field is also stronger on the inboard side than on the outboard side, which is typically the case, then the downward force on the inboard side ($\mathbf{J}_P \times \mathbf{B}_T$) will be stronger than the corresponding upward force on the outboard side, thereby producing a net downward (restraining) force.

In order to formulate this effect mathematically, we note that the poloidal current density in the arched rope will fall off as $1/R$. Ampère's Law indicates that the resulting toroidal will also fall off as $1/R$. Thus we can write

$$J_P \rightarrow -\left(\frac{R_0}{R}\right) J_P(r)\sin\theta \quad \text{and} \quad B_T \rightarrow \frac{R_0}{R}\, B_T(r). \tag{14}$$

The next step is to integrate $f_t = -J_P B_T$ over the apex wedge of the flux rope according to Eq. (4)

$$F_t = \frac{1}{R_0}\int_0^{2\pi} d\theta \int_0^a dr \left[r\, R \left(\frac{R_0}{R}\, J_P \sin\theta\right)\left(\frac{R_0}{R}\, B_T\right)\right]. \tag{15}$$

Here, we have assumed a curvilinear scale factor of $h_T = R$. Canceling factors and making the large aspect ratio assumption that $r \ll R_0$, the above equation reduces to

$$F_t = \frac{1}{R_0}\int_0^{2\pi} d\theta \int_0^a dr \left[r\left(R_0 \sin\theta - r\sin^2\theta\right) J_P B_T\right]. \tag{16}$$

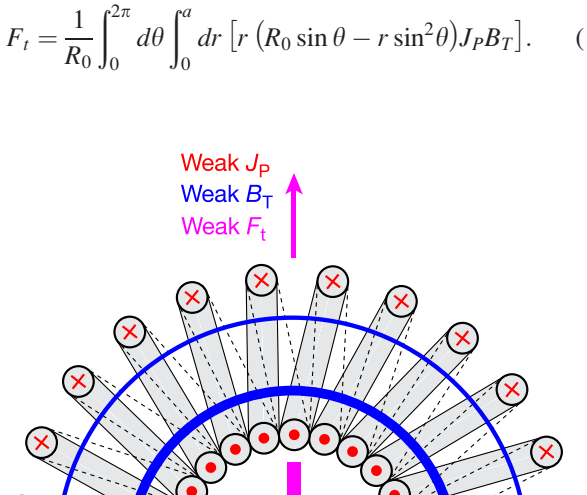

FIG. 5. A helical coil demonstrates the nature of the toroidal field tension force. The increased poloidal current density J_P on the inboard side of the coil produces a contraction force ($J_P \times B_T$) that is stronger than the corresponding expansion force on the outboard side of the coil. This asymmetry results in a net contraction force on the flux rope.

The integral over θ eliminates the $\sin\theta$ term, leaving

$$F_t = -\frac{\pi}{R_0}\int_0^a dr\, r^2 J_P(r)\, B_T(r). \tag{17}$$

From Ampére's Law, $J_P = -\partial B_T/\partial r$ such that

$$F_t = -\frac{\pi}{R_0}\int_0^a dr \left[r B_T^2 - \frac{1}{2}\frac{\partial}{\partial r}\left(r^2 B_T^2\right)\right], \tag{18}$$

which reduces to

$$F_t = -\frac{1}{2}\frac{\pi a^2}{\mu_0 R_0}\left[\langle B_T^2\rangle - B_{g0}^2\right], \tag{19}$$

where $\langle B_T^2\rangle$ is the cross-section-averaged square of the total toroidal field, and we have assumed that the toroidal field at the edge of the rope ($r = a$) is simply the external guide field B_{g0}. From this result, we see that a paramagnetic internal toroidal field will increase $\langle B_T^2\rangle$ relative to B_{g0}^2 and therefore, produce a downward restraining force on the rope. Furthermore, though no assumption was made during this derivation that F_t would be a tension force, the final result takes exactly the form of a tension term with $F_t \sim B_T^2/R$. For convenience, we can rewrite the above equation as

$$F_t = -\frac{1}{2}\left(\frac{\mu_0 I_T^2}{4\pi R_{sc}}\right)\left[\frac{\langle B_T^2\rangle - B_{g0}^2}{B_{Pa}^2}\right], \tag{20}$$

where $B_{Pa} \equiv \mu_0 I_T/2\pi a$ is the edge poloidal field. What remains to be constrained is the amplitude of the paramagnetic toroidal field that causes $\langle B_T^2\rangle$ to exceed B_{g0}^2 in Eq. (20) and therefore generates a downward toroidal field tension force.

b. The plasma-generated paramagnetic toroidal field. The physical mechanism that lies at the heart of the toroidal field force is the paramagnetic toroidal field B_{Ti} that is generated by the plasma in the core of the line-tied flux rope. Without this internal toroidal field and its corresponding poloidal currents, the toroidal field forces described in Eq. (13) would vanish. The origin of the plasma-produced paramagnetic field can be understood heuristically through simple minor radius force balance arguments. The toroidal current flowing in the flux rope generates a minor radius pinch force that must be balanced by either thermal or magnetic field pressure. In a zero-β system, the only available source for this back pressure is the toroidal magnetic field. The presence of a vacuum toroidal field alone is not sufficient because the vacuum field is current-free. Instead, in the process of relaxing to a force-free state, poloidal currents are induced in the plasma that generate a paramagnetic toroidal field in the core of the rope. It is these poloidal currents that interact with the toroidal field to oppose the minor radius pinch force produced by the toroidal plasma current.

In order to quantitatively analyze the paramagnetic toroidal field, we now use a 1D linear screw pinch model to derive an expression for B_{Ti}. This 1D flux rope model assumes that the rope is an infinite cylinder with minor radius a carrying a "toroidal" current I_T along a uniform

external guide field $B_g = B_{g0}$. The only variation in this 1D model is along the minor radial coordinate r. In order for a zero-β linear screw pinch to be force-free, the magnetic forces directed along this minor radius must cancel

$$\begin{aligned} 0 &= \mathbf{J}_T \times \mathbf{B}_P + \mathbf{J}_P \times \mathbf{B}_T \\ &= -J_T B_P + J_P B_T. \end{aligned} \tag{21}$$

Here, the first term represents the pinch effect from the toroidal current and the second term represents the back pressure from the plasma-generated paramagnetic toroidal field. Ampére's law can be used to eliminate currents in favor of fields, giving

$$J_T B_P = \frac{1}{\mu_0}\left(\frac{\partial B_P}{\partial r} + \frac{B_P}{r}\right) B_P, \tag{22}$$

$$J_P B_T = \frac{1}{\mu_0}\left(-\frac{\partial B_T}{\partial r}\right) B_T. \tag{23}$$

Equating the two, multiplying through by $2r^2$, and recasting the derivatives gives

$$2rB_T^2 - \frac{\partial}{\partial r}\left(r^2 B_T^2\right) = \frac{\partial}{\partial r}\left(r^2 B_P^2\right), \tag{24}$$

which can be integrated over the cross-section of the flux rope to get

$$\langle B_T^2 \rangle - B_{g0}^2 = B_{Pa}^2. \tag{25}$$

Here, we have again assumed that the toroidal field at the edge of the flux rope is the guide field B_{g0}. This simple relationship allows us to write the paramagnetic toroidal field B_{Ti} in terms of the "known" parameters B_{g0} and B_{Pa}. Substituting $B_T = B_{g0} + B_{Ti}$ into Eq. (25) and solving for $\langle B_{Ti} \rangle$ gives

$$\langle B_{Ti} \rangle = \gamma^{-1}\left(\sqrt{B_{g0}^2 + \gamma B_{Pa}^2} - B_{g0}\right), \tag{26}$$

where $\gamma \equiv \langle B_{Ti}^2 \rangle / \langle B_{Ti} \rangle^2$ is a parameter of order unity that varies with the internal radial profile of $B_{Ti}(r)$. In Section V, Eq. (26) will be compared directly with experimental measurements in order to test the assumptions made in this derivation of B_{Ti}.

c. Connection to the hoop force. A final interesting result can be obtained by combining Eqs. (20) and (25)

$$F_t \simeq -\frac{1}{2}\left(\frac{\mu_0 I_T^2}{4\pi R_0}\right). \tag{27}$$

This expression is both independent of B_g and directly compatible with the hoop force expression in Eq. (6). Thus, the analytical expression for the tension force can be thought of as an offset to the hoop force

$$F_h + F_t = +\frac{\mu_0 I_T^2}{4\pi R_0}\left[\ln\left(\frac{8R}{a}\right) - \frac{3}{2} + \frac{\ell_i}{2}\right], \tag{28}$$

where the $-1/2$ from the tension force is folded into the $-3/2$ in this expression. We see here that the tension effect is minimal in the large aspect ratio limit where the $\ln(8R/a)$ term dominates. In the low aspect ratio limit that is applicable here, on the other hand, the $-3/2$ vs. -1 term can be quite important.

Over the course of this subsection, analytical expressions have been derived for the hoop, strapping, and toroidal field forces that are expected to contribute to the equilibrium force balance at the flux rope apex. The results of these derivations are summarized in Table II. This three part decomposition of apex forces is by no means unique. We believe, however, that this particular decomposition provides the best opportunity to understand the physics that govern line-tied flux rope equilibria.

C. The torus and kink instabilities

As described in the introduction, one of the primary motivations for studying the forces acting on a line-tied flux rope is to understand the onset criterion for loss-of-equilibrium-driven solar eruptions. The loss-of-equilibrium has recently been formulated in terms of an ideal magnetohydrodynamic instability called the torus instability.[10–14,25–27] The basic idea of the torus instability is that an outward perturbation of the flux rope will be unstable if the overlying strapping field decays sufficiently quickly with height above the photosphere. The instability occurs because the restoring forces provided by the strapping field are too weak to prevent further expansion.

In the standard torus instability derivation,[10] which was originally carried out for laboratory fusion devices,[15] the key instability criterion is based on the vacuum field decay index n

$$n(z) \equiv -\frac{z}{|\mathbf{B}_{vac}|}\frac{\partial |\mathbf{B}_{vac}|}{\partial z} > \frac{3}{2}, \tag{29}$$

where $\mathbf{B}_{vac}$ is the vacuum magnetic field and z is the height above the photosphere. This $n > 3/2$ instability criterion is derived in the large aspect ratio limit by equating the hoop and strapping force expressions from Eqs. (6) and (11),

TABLE II. Summary of source terms and analytical expressions for the forces acting on the flux rope apex. The hoop force expression comes from combining Eq. (6) with the shifted-circle radius in Eq. (9). The hoop force corrections are the sub-surface current path corrections introduced in Section II B 2. The strapping force expression comes from Eq. (11), while the two tension force expressions come from Eqs. (20) and (27), respectively.

Force	Source term	Analytical expression
Poloidal field hoop force (upward)	$f_h = +J_T B_{Pi}$	$F_h(z) = +\frac{\mu_0 I_T^2}{4\pi R_{sc}}\left[\ln\left(\frac{8R_{sc}}{a}\right) - 1 + \frac{\ell_i}{2}\right] + \text{corr.}$
Poloidal field strapping force (downward)	$f_s = -J_T B_s$	$F_s(z) = -I_T B_{s0}$
Toroidal field tension force (downward)	$f_t = -J_P B_T$	$F_t(z) = -\frac{1}{2}\left(\frac{\mu_0 I_T^2}{4\pi R_{sc}}\right)\left[\frac{\langle B_T^2 \rangle - B_{g0}^2}{B_{Pa}^2}\right] \simeq -\frac{1}{2}\left(\frac{\mu_0 I_T^2}{4\pi R_{sc}}\right)$

respectively. One must also assume that the toroidal current evolution is governed by poloidal flux conservation.[10,15,17] The $n > 3/2$ instability criterion is a remarkably concise result given the complexity of the system. That being said, the assumptions of infinite aspect ratio and toroidal symmetry substantially impact the final result. Olmedo and Zhang,[19] for instance, have considered the impact of line-tying on the torus instability, much as we have considered its impact on the hoop force in Section II B 2. Their findings await validation.

A second magnetohydrodynamic instability to which line-tied magnetic flux ropes are susceptible is the current-driven external kink instability. Originally treated by Kruskal and Schwarzschild[28] and Shafranov[29] in the context of laboratory fusion devices, the kink has long been studied as a candidate solar eruption mechanism.[30–37] It is a global instability that arises when the magnetic field lines at the edge of the flux rope are sufficiently twisted such that they resonate with helical $n \geq 1$ perturbations to the rope (here n is the axial/toroidal mode number). This leads to the so-called Kruskal-Shafranov instability criterion, which is traditionally written in terms of the edge safety factor q_a

$$q_a \equiv \frac{2\pi}{\iota_a} = \frac{2\pi a}{L}\frac{B_{Ta}}{B_{Pa}} < 1. \tag{30}$$

Here, ι_a is the rotational transform, which measures the field line twist along the length of the flux rope. Specifically, ι_a represents the number of poloidal radians traversed by a field line as it runs from one end of the flux rope to the other.[38] The other quantities in Eq. (30) are as follows: a is the flux rope minor radius, L is the flux rope length, B_{Ta} is the edge toroidal field, and $B_{Pa} \equiv I_T/2\pi a$ is the edge poloidal field. Note that increasing toroidal field and minor radius are stabilizing, while increasing poloidal field and length are destabilizing.

The instability criteria in Eqs. (29) and (30) indicate that the field decay index n and the edge safety factor q_a are two key instability control parameters. As such, these two parameters define a two-dimensional n vs. q_a instability parameter space over which flux rope eruptivity can be studied. The laboratory experiments described in this paper were specifically designed to explore this instability of parameter space in detail. Thus, while the kink instability has previously been studied in both linear[39–41] and arched[42] flux rope experiments, the experiments reported here are the first to study the torus instability and its relationship to the kink.

III. LABORATORY FLUX ROPE EXPERIMENTS IN THE MAGNETIC RECONNECTION EXPERIMENT

The laboratory experiments presented in this paper are conducted in the Magnetic Reconnection Experiment (MRX) at Princeton Plasma Physics Laboratory.[43] For these experiments, a novel apparatus was designed and constructed to function as an insert to the MRX vacuum chamber. It produces both the vacuum (potential) magnetic field in which the flux rope is embedded and the flux rope plasma itself. One of the most important features of this experiment is its separation of timescales, which emulates the conditions of the solar corona. This separation of timescales (dynamic $\ll$ driving $\ll$ dissipation) is a key tenet of the storage-and-release eruption paradigm described in Section I. In our experiments, the dynamic timescale of the plasma (the Alfvén transit time τ_A) is $\tau_A \simeq 3\,\mu$s, while the driving timescale τ_D over which the plasma current is injected is $\tau_D \simeq 75$–$300\,\mu$s, and the dissipation timescale (the resistive decay time τ_R) is $\tau_R \gtrsim 500\,\mu$s such that $\tau_A \ll \tau_D \ll \tau_R$. As such, the line-tied flux ropes produced in MRX persist in a quasi-statically evolving equilibrium for many Alfvén transit times. It should be noted that laboratory experiments have been carried out in other devices to study the dynamics of a magnetized plasma arc.[44,45] However, these experiments had only limited magnetic diagnostics, and it was unclear that the arcs were long-lived compared to the Alfvén time. A more recent experiment that uses laser-produced plasmas at the footpoints of a stable arc to drive an eruption[46] is essentially testing a mass injection model for eruption onset. Neither of these experimental approaches achieves the separation of timescales required to study the storage-and-release behavior that we seek in the MRX flux rope experiments.

A. Experimental setup

Magnetic flux ropes are formed in MRX by generating an arc discharge along arched field lines connecting two upward-facing electrodes (see Fig. 6(a)). In order to enforce the requisite magnetic field line-tying at the flux rope footpoints, the electrodes are constructed from highly conducting metals such as copper that lock in the vacuum magnetic field for the duration of the discharge. The plasma region in these experiments ($z > 0$) is physically separated from the potential field coil region ($z < 0$) by an insulating glass substrate. Prior to initiating the discharge, a static vacuum (potential) magnetic field is generated by driving current in four independently controlled magnetic field coil sets (orange and blue in Fig. 6(a)). These coil sets are directly analogous to the subsurface currents that produce sunspots and their associated potential fields in the corona. By tuning the currents in the various coils, vacuum field configurations with a wide range of solar-relevant parameters can be produced.

Once the vacuum magnetic field has been generated, a small amount of neutral gas (5–20 mTorr) is injected both at the vessel wall and in the center of the cathode (i.e., the footpoint that is negatively biased). The gas injection at the cathode is key for breaking down the plasma at reasonable fill pressures. Typically, hydrogen or helium is used due to their low mass and corresponding high degree of magnetization. In order to initiate the discharge, a capacitor bank is connected across the electrodes, and the plasma breaks down along the magnetic field lines that intersect the electrodes. The current in the flux rope rises quasi-statically as the energy stored in the capacitor bank is converted into magnetic energy that twists up the flux rope. A typical flux rope discharge in MRX lasts for approximately a millisecond. This timescale is set by the combined inductance and capacitance of the series capacitor bank and plasma arc circuit. The peak plasma current ranges from 10 to 25 kA, depending on the voltage applied to the driving capacitor bank. This amount of current is sufficient to produce non-potential magnetic fields of 300–500 G. Fields of this strength substantially

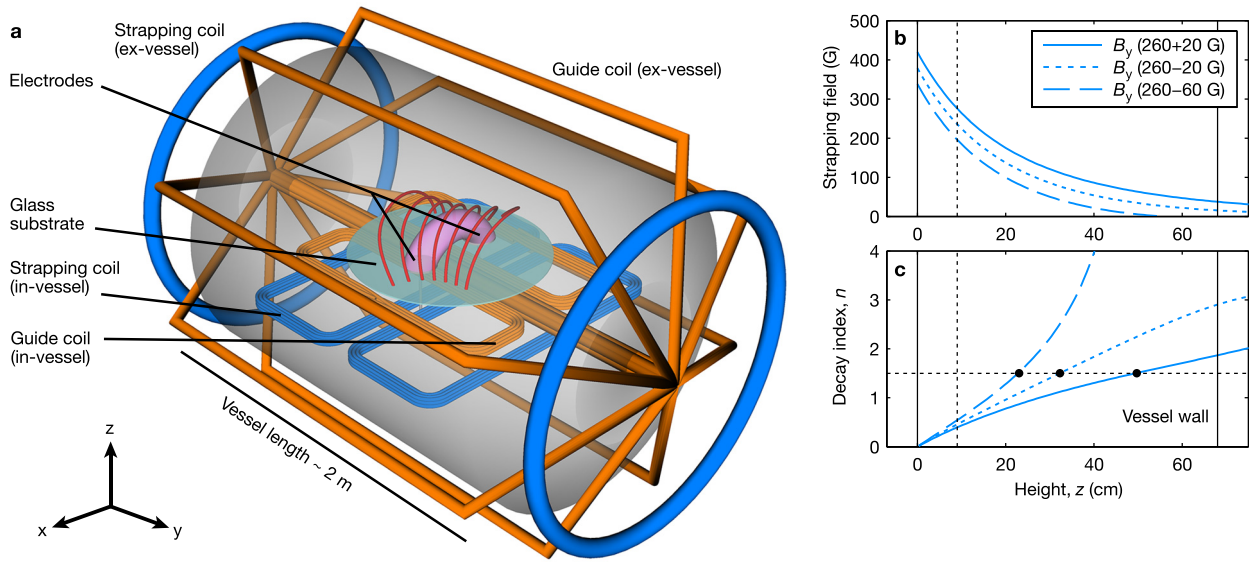

FIG. 6. Experimental setup for studying arched, line-tied magnetic flux ropes in the Magnetic Reconnection Experiment (MRX). (a) A plasma arc (pink) is maintained between two copper electrodes connected to a capacitor bank. The plasma arc is formed within a vacuum (potential) magnetic field configuration that is generated by four independently controlled magnetic field coil sets (orange and blue). Two of the coil sets produce a guide magnetic field along the flux rope arch, while the other two produce a strapping field orthogonal to the flux rope arch. These various field contributions combine to produce an obliquely aligned vacuum field arcade (red) in which the flux rope is embedded. Reproduced with permission from Myers *et al.*, Nature **528**, 526 (2015). Copyright 2015 Nature Publishing Group. (b) Demonstration of how the two strapping field coil sets are used to tune the field decay index in the experiment. In this numerically calculated example, the in-vessel strapping coils provide +260 G of strapping field at $z \simeq 10$ cm, while the ex-vessel coils provide a spatially uniform offset of +20, −20, or −60 G. Note that the vessel wall is located at $z_w \simeq 68$ cm. (c) The corresponding field decay index profiles for the three strapping field profiles shown in (b). In this way, the height of the $n = 3/2$ point can be systematically varied.

modify the applied vacuum field configuration, thereby forming non-potential equilibria, and, under certain conditions, driving eruptive instabilities that are directly relevant to events in the solar corona.

In order to study the torus and kink instabilities in these experiments, it is imperative that we are able to independently tune both the strength and the gradient of the externally applied guide and strapping fields. The selection of the desired vacuum field parameters (B_g, B_s, n, etc.) is accomplished by selecting the individual currents that are driven in the four sets of vacuum magnetic field coils shown in Fig. 6(a). To demonstrate the technique that is used for tuning a given field component, we focus in Figs. 6(b) and 6(c) on the strapping field coils. In this example, the prevailing strapping field is provided by the in-vessel strapping coils. The currents in these two rectangular coils are configured so that the strapping field lines arch up out of one coil and back down into the other. In order to tune the decay index of the strapping field, a small amount of current is driven in the large ex-vessel Helmholtz strapping coils. This produces a spatially uniform offset to the strapping field that either enhances or cancels a portion of the prevailing field from the in-vessel strapping coils. In Fig. 6(b), sample strapping field profiles are shown with +260 G of forward field and three different reverse field values (+20 G, −20 G, and −60 G). We see that even though the reverse field values constitute only a perturbation to the forward field, they substantially alter the strapping field decay index profile (Fig. 6(c)). This magnetic field superposition technique, which was verified with hall probe measurements (not shown), is used to tune both the guide and the strapping fields in the experiment.

B. Plasma parameters

While a laboratory experiment cannot directly simulate the enormous scales of the solar atmosphere, we can establish the similarity of the relative values of a number of important parameters. The first task is to identify the parameters achieved in the laboratory, which are summarized in Table III. Here, the magnetic field strength B is directly measured, the neutral density n_n is estimated from the fill pressure, and the plasma density n_e and temperature T_e are estimated from Langmuir probe measurements. The Alfvén velocity v_A follows from the magnetic field and density values, and the various timescales have already been discussed.

For a line-tied plasma to be in the MHD regime, the following two conditions must be met: (1) the ion gyro-radius ρ_i must be much smaller than the flux rope cross-sectional radius a; and (2) the electron-ion mean free path λ_{ei} must be

TABLE III. Plasma parameters in the MRX flux rope experiments. Reprinted with permission from Myers *et al.*, Nature **528**, 526 (2015). Copyright 2015 Nature Publishing Group.

Laboratory parameter	Symbol	Value	Units
Magnetic field strength	B	300–500	G
Neutral density (approx.)	n_n	$\sim 5 \times 10^{14}$	cm^{-3}
Electron density (approx.)	n_e	$0.5–1 \times 10^{14}$	cm^{-3}
Electron temperature (approx.)	T_e	3–5	eV
Flux rope scale length	L	0.5	m
Alfvén velocity	v_A	65–150	km/s
Alfvén transit time	τ_A	3–8	μs
Footpoint driving time	τ_D	~150	μs
Resistive diffusion time (Spitzer)	τ_R	0.8–2	ms

much shorter than the plasma length L. As is well known, both of these conditions are met for a typical solar flux rope. In Table IV, we show that these conditions are also satisfied for our laboratory flux ropes. Additionally, the Lundquist number $S \equiv \mu_0 L v_A/\eta$, where L is the characteristic system size and η is the electrical resistivity of the plasma, should be much larger than unity. In the experiment, $S \sim 100$–500, indicating that the magnetic field is largely frozen in to the plasma. This parameter is important for simulating solar flux ropes, where S ranges from 10^4 in the chromosphere to 10^{12} in the corona.

An additional experimental consideration is the effect of neutral particles that are not ionized during the discharge. Given the fill pressures used and the approximate plasma densities achieved, the electron-ion mean free path $\lambda_{ei} \lesssim 1$ cm is at least an order of magnitude shorter than the electron-neutral mean free path $\lambda_{en} \gtrsim 10$ cm. This means that, despite the presence of background neutrals, the ionized plasma dominates the experimental dynamics. Furthermore, the role of neutrals can be tested experimentally by increasing the fill pressure and quantifying how the observed phenomena are affected. Minimal changes were observed over more than an order of magnitude in fill pressure.

C. Diagnostics

The MRX flux rope plasmas are primarily diagnosed with two key systems: (1) fast visible light cameras that image the plasma from multiple angles; and (2) an *in situ* magnetic probe array that measures the internal magnetic structure of the plasma. Images from the fast cameras, which are used to qualitatively assess the plasma performance, can be seen in Refs. 17 and 18. The results presented in this paper are derived instead from the high-coverage magnetic probe array. Such magnetic probe arrays are routinely deployed in MRX to acquire magnetic field data over a two-dimensional cross-section of the plasma. The probes are constructed from miniature ($\sim$2 mm) magnetic pickup coils with $\sim$100 turns each. The pickup coils are mounted in orthogonal triplets to measure all three components of the vector magnetic field at each location. These triplets are distributed at 4 cm intervals inside long, thin glass tubes (7 mm OD) that serve as the plasma-facing components. The raw $\dot{B}$ signals are processed through custom integrator circuits before being sent to 2.5 MHz high-speed digitizers.

TABLE IV. Dimensionless parameter comparison between the MRX flux rope experiments and the solar corona. Here, MFP is the electron mean free path λ_{ei}. Reprinted with permission from Myers *et al.*, Nature **528**, 526 (2015). Copyright 2015 Nature Publishing Group.

Dimensionless parameter	Symbol	Solar	Laboratory
Driving/Alfvén time	τ_D/τ_A	100–10^4	20–50
Driving/resistive time	τ_D/τ_R	10^{-7}	$\sim$0.1
Ion gyroradius/minor radius	ρ_i/a	10^{-6}	0.05
MFP/plasma length	λ_{ei}/L	10^{-2}	10^{-3}–10^{-2}
Lundquist number	S	10^4–10^{12}	100–500
Ionization fraction	$n_e/(n_n+n_e)$	50%–100%	10%–20%
Plasma beta	β	$\sim$1%	2%–20%

For the flux rope experiments presented here, a new two-dimensional magnetic probe array was constructed to have unprecedented areal coverage (24 cm $\times$ 64 cm) and a fine spatial resolution of 4 cm (see Fig. 7). As such, more than 300 pickup coils provide *in situ* vector magnetic field data at more than 100 locations within the plasma. A key feature is that the probe array can be rotated arbitrarily about the z-axis between discharges (see Fig. 7). This means that the cross-section of the probe array can be aligned at any orientation with respect to the flux rope. The two orientations featured here are the toroidal and poloidal cross-sections of the flux rope (see Figs. 7(a) and 7(b), respectively).

The vector/color plots on the right hand side of Fig. 7 show a single-time snapshot of the magnetic field within the flux rope. In each case, the vectors represent the in-plane field, while the colors represent the out-of-plane field. For the poloidal field components, the total poloidal field $\mathbf{B}_P = \mathbf{B}_s + \mathbf{B}_{Pi}$ is displayed. For the toroidal field components, on the other hand, the vacuum fields are omitted in order to emphasize the structure of the plasma-generated toroidal fields $\mathbf{B}_{Ti}$. One key measurement that can be extracted from these magnetic field data is the vertical

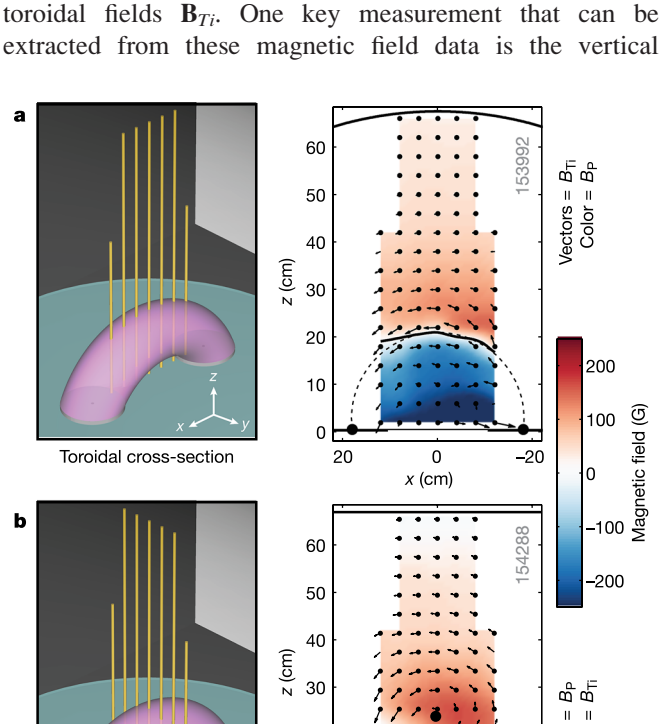

FIG. 7. The *in situ* magnetic probe array used to diagnose the internal magnetic structure of the plasma. (a) Schematic and representative data acquired with the probe array aligned in the toroidal (x-z) cross-section of the flux rope. In this case, the vectors represent the in-plane toroidal magnetic field produced by the plasma $\mathbf{B}_{Ti} \approx B_{xi}\hat{\mathbf{e}}_x + B_{zi}\hat{\mathbf{e}}_z$, while the color represents the total out-of-plane poloidal magnetic field $B_P = \hat{\mathbf{e}}_y \cdot \mathbf{B}$. This out-of-plane field reverses sign at the magnetic axis of the flux rope. (b) Schematic and representative data acquired with the probe array aligned in the poloidal (y-z) cross-section of the flux rope. In this case, the vectors represent the in-plane total poloidal field $\mathbf{B}_P$, while the color presents the out-of-plane toroidal field produced by the plasma $B_{Ti} = \hat{\mathbf{e}}_x \cdot \mathbf{B}_i$. B_{Ti} is always paramagnetic with respect to the background guide field B_g. Reproduced with permission from Myers *et al.*, Nature **528**, 526 (2015). Copyright 2015 Nature Publishing Group.

position of the flux rope magnetic axis. This position is defined as the location where the poloidal magnetic field reverses sign. For the examples in Fig. 7, the measured magnetic axis position is shown as a solid black line in Fig. 7(a) and a black dot in Fig. 7(b). This capability will be used in Sec. III D to analyze the flux rope height under a variety of experimental conditions.

A second key feature of the magnetic field data is the direct measurement of the internal toroidal field $\mathbf{B}_{Ti}$. The magnetic field data show that $\mathbf{B}_{Ti}$ has the following properties: (1) $\mathbf{B}_{Ti}$ is bundled in the core of the flux rope; and (2) $\mathbf{B}_{Ti}$ is paramagnetic, or co-directed, with respect to the vacuum toroidal guide field $\mathbf{B}_g$. These properties are demonstrated most clearly in Fig. 8, which shows magnetic measurements of $\mathbf{B}_{Ti}$ from two sample flux rope discharges. In each case, the guide field, which is not shown, arches from right to left. Correspondingly, the measured $\mathbf{B}_{Ti}$ vectors also arch from right to left, confirming that the plasma-produced $\mathbf{B}_{Ti}$ is paramagnetic. Furthermore, the color, which shows $B_T = \hat{\mathbf{e}}_T \cdot \mathbf{B}_{Ti}$, demonstrates that the B_{Ti} is bunched in the core of the flux rope. Note that the B_{Ti} in one sample discharge is substantially more intense than in the other. The difference is that the strength of B_g is different in the two cases, with the strong B_g case corresponding to weak B_{Ti} and vice-versa. This inverse relationship between B_g and B_{Ti} at fixed B_{Pa} is consistent with Eq. (26).

D. Key results on the torus and kink instabilities

The final step is to summarize the key results on flux rope eruptivity that provide the motivation to study the flux rope forces in detail. These results were originally reported in Ref. 18, where the torus versus kink (n vs. q_a) instability parameter space was explored using the MRX flux rope experiments. Four different instability regimes are identified, with one of them—the so-called failed torus regime—constituting a new discovery. The conclusion, as summarized below, is that a previously unknown dynamic enhancement of the toroidal field tension force can prevent torus-unstable flux ropes from erupting. This measured dynamic enhancement of the tension force is attributed to non-ideal magnetic self-organization events in the flux rope plasma.[18]

Flux rope eruptivity is best quantified by studying the height-time evolution of the flux rope's magnetic axis. Fortunately, as described in Sec. III C, the magnetic measurements from the probe array can be used to track the apex height of the flux rope, $z_{ap}(t)$, as a function of time. Four sample height-time traces are shown in Fig. 9. In particular, each subpanel in Fig. 9(b) shows $z_{ap}(t)$ as a black line along with the poloidal magnetic field measured along the central probe in the probe array $B_y(t, z)$, which is shown in color. In each plot, the magnetic axis position is the location where the poloidal field reverses sign.

The four sample discharges shown in Fig. 9(b) are chosen because they represent the four stability regimes identified in the MRX flux rope experiments.[18] These stability regimes, which are labeled as stable, eruptive, failed kink, and failed torus, are delineated by different values of the torus and kink instability control parameters n and q_a (see Section II C). These two control parameters are scanned independently by modifying the strength and spatial variation of the applied vacuum field configuration as described in Section III A. We note here that it would also be possible to control q_a by varying the plasma current, but in practice the plasma current is held fixed (see Fig. 9(a)) due to experimental considerations. For the four sample discharges in Fig. 9, the achieved values of the instability control parameters n and q_a are listed in the table in Fig. 9(c). These scalar values

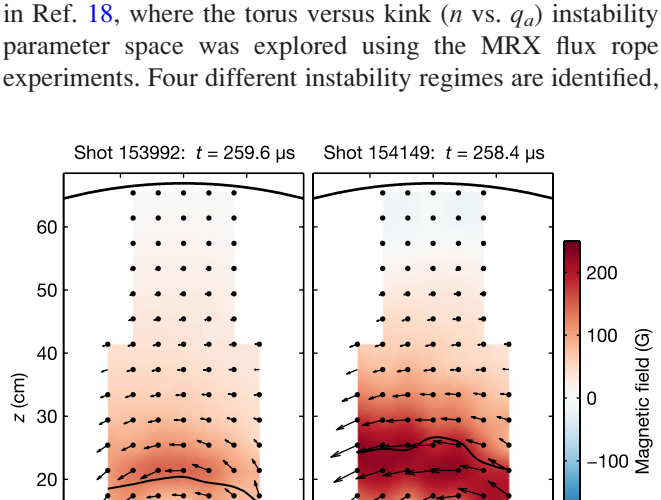

FIG. 8. Two sample magnetic measurements of the plasma-produced internal toroidal field $\mathbf{B}_{Ti}$ (vectors and color). In each case, the $\mathbf{B}_{Ti}$ vectors arch from right to left, which makes them paramagnetic, or co-directed, with the applied vacuum guide field $\mathbf{B}_g$ (not shown). Additionally, the magnitude of $\mathbf{B}_{Ti}$ (color), is largest near the magnetic axis (the black line). The magnitude of $\mathbf{B}_{Ti}$ is weaker in the case on the left than in the case on the right. The difference between the two is the strength of the applied guide field, which is strong in the left hand case and weak in the right hand case.

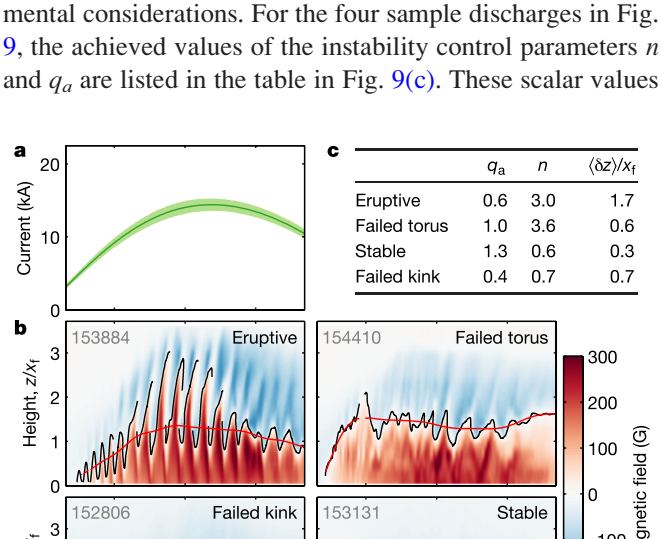

	q_a	n	$\langle \delta z \rangle / x_f$
Eruptive	0.6	3.0	1.7
Failed torus	1.0	3.6	0.6
Stable	1.3	0.6	0.3
Failed kink	0.4	0.7	0.7

FIG. 9. Temporal evolution of the flux rope apex height $z_{ap}(t)$ in four different stability regimes. (a) Mean plasma current waveform (green) and its standard deviation (the lighter green band). Each discharge has the same nominal plasma current. (b) Flux rope apex height waveforms (black lines) along with the poloidal field measurements $B_y(t, z)$, from which the apex height is measured. (c) Table of key parameter values for these four discharges. Reproduced with permission from Myers *et al.*, Nature **528**, 526 (2015). Copyright 2015 Nature Publishing Group.

are determined by evaluating Eqs. (29) and (30) for the flux rope parameters achieved in a given discharge. In particular, n and q_a are evaluated at the maximum of the temporally filtered apex height $\langle z_{ap}(t)\rangle$ which is shown in red in each subpanel of Fig. 9(b). Additional details of the evaluation of n and q_a can be found in Ref. 18.

The four different sample discharges in Fig. 9(b) behave qualitatively different from each other. The magnetic axis in the stable discharge remains steady throughout the lifetime of the plasma, while the eruptive discharge rapidly and repeatedly erupts toward the wall of the chamber, which is located at the top of each plot (at $z/x_f \simeq 3.8$). The two "failed" regimes, which will be discussed shortly, show intermediate behavior with small-scale spatial oscillations but no catastrophic eruptions. In order to quantify these disparate behaviors, we introduce a metric called the normalized instability amplitude $\langle \delta z\rangle/x_f$. Here, the instability amplitude $\langle \delta z\rangle$ is defined as the maximum of the envelope of the dynamic spatial oscillations about the equilibrium position of the flux rope $\langle z_{ap}(t)\rangle$. The quantity $\langle \delta z\rangle$ is then normalized to half of the footpoint separation distance $2x_f$ such that a flux rope with $\langle \delta z\rangle/x_f \sim 1$ oscillates vertically on the scale of the footpoint major radius. Values less than 0.5 are clearly stable, while values above unity are clearly eruptive. Later in this paper, $\langle \delta z\rangle/x_f = 0.8$ is used to delineate non-erupting flux ropes from those that erupt. The specific values of $\langle \delta z\rangle/x_f$ for the four cases in Fig. 9(b) are listed in Fig. 9(c), showing that the normalized instability amplitude provides a quantitative assessment of the qualitatively disparate behaviors in Fig. 9(b).

The remaining task is to examine how the instability amplitude varies over the broader n vs. q_a instability parameter space. In Fig. 10, the results of more than 800 flux rope discharges are combined into a single scatterplot of flux rope eruptivity. Each data point is the mean of 2–5 plasma discharges taken under identical experimental conditions. The four stability regimes identified in Fig. 9 are observed across the instability parameter space in Fig. 10. As expected,

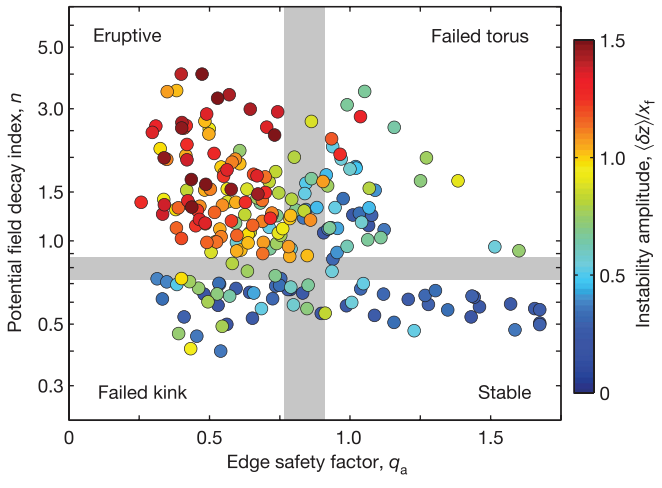

FIG. 10. The experimentally measured flux rope instability parameter space. Four distinct instability regimes are identified, with the empirical stability boundaries shown in gray. While the stable, eruptive, and failed kink regimes are expected, the failed torus regime constitutes a new discovery. Reproduced with permission from Myers *et al.*, Nature **528**, 526 (2015). Copyright 2015 Nature Publishing Group.

the stable regime in the bottom right is stable to both the kink and the torus instabilities, while the eruptive regime in the top left is unstable to both. The failed kink regime in the bottom left is kink unstable but torus stable, and it does not produce eruptions. This result, which is consistent with numerical simulations of line-tied flux ropes,[36] confirms that the onset of the kink instability does not necessarily lead to an eruption.

The failed torus regime in the top right of Fig. 10, on the other hand, constitutes an entirely new discovery. Here, torus unstable flux ropes fail to erupt. Detailed measurements of the flux rope forces presented in Ref. 18 show that the toroidal field tension force is dynamically enhanced in this regime, thereby preventing flux rope eruptions. One of the purposes of this paper is to fully develop and validate the force measurement techniques that are used to identify the dynamically enhanced toroidal field tension force in Ref. 18. Additional analysis of the evolution of the poloidal and toroidal fluxes shows that the dynamically enhanced tension force is a result of magnetic self-organization events that conserve magnetic helicity within the flux rope.[18]

We note that observed torus and kink instability thresholds of $n \sim 0.8$ and $q_a \sim 0.8$ (shown in gray in Fig. 10) differ from the theoretically predicted values of $n = 3/2$ and $q_a = 1$. The reduced kink threshold is consistent with numerical simulations of line-tied flux ropes.[31–37] The reduced torus threshold is perhaps more interesting. It calls into question whether the analytical force models that are used to derive the $n = 3/2$ torus threshold are representative of the flux rope forces in the line-tied, low-aspect-ratio conditions of the laboratory and coronal flux ropes. This interesting result motivates the detailed study of flux rope forces that follows. Unlike in Ref. 18, the focus here is on the measurement of quasi-steady (equilibrium) forces that feed into loss-of-equilibrium calculations of flux rope stability.

IV. LABORATORY MEASUREMENTS OF MAGNETOHYDRODYNAMIC FORCES

In this section, we use the internal magnetic field data acquired from the MRX line-tied flux rope experiments to directly measure the $\mathbf{J} \times \mathbf{B}$ force terms acting on the flux rope plasma. These measurements provide the necessary information to both evaluate the flux rope equilibrium force balance and validate (or invalidate) the analytical force expressions derived in Section II. We begin by describing in detail the laboratory force measurement procedure that has been developed for the MRX flux rope experiments. The goal of the flux rope force analysis, which is carried out on data acquired with the probe array aligned in the poloidal (y-z) plane of the flux rope (see Fig. 7), is to measure the integrated force per unit length $F(z_{ap})$, acting on the flux rope apex (see Fig. 1). The formal expression for the integration of $F(z_{ap})$ is given in Eq. (4). In order to use this formulation to directly measure the flux rope forces from the experiment, we must determine several key quantities including the toroidal scale factor $h_T(z)$ and the in-plane boundary of the flux rope $r = a(\theta)$.

Identifying the toroidal scale factor $h_T(z)$ is an involved process wherein magnetic field data from various configurations

are used to measure the toroidal curvature of the flux rope. The details of this procedure are described in Appendix A. In short, an ensemble of flux rope discharges is used to determine an average toroidal scale factor that can be applied to many flux rope discharges with similar experimental conditions (e.g., they have the same footpoint separation distance, $2x_f$). In cases where a directly measured toroidal curvature is not available, the line-tied curvature from the shifted-circle model (Eq. (9)) is used instead.

With the toroidal scale factor in hand, the next task is to gather all components of the magnetic field **B** and the current density **J** that are needed to compute the various force density terms f_i. All three components of the magnetic field are directly measured by the magnetic field probe array. From these magnetic field measurements, the various components of the current density can be computed as

$$\mathbf{J}_P = \frac{1}{\mu_0}\left[\frac{1}{h_T}\frac{\partial\left(h_T B_{Ti}\right)}{\partial z}\right]\hat{\mathbf{e}}_y - \frac{1}{\mu_0}\left[\frac{\partial B_{Ti}}{\partial y}\right]\hat{\mathbf{e}}_z,$$
$$J_T = \frac{1}{\mu_0}\left[\frac{\partial B_{zi}}{\partial y} - \frac{\partial B_{yi}}{\partial z}\right]. \tag{31}$$

These current densities, along with their corresponding magnetic fields, are plotted for a sample time slice in Fig. 11. The sample discharge from which this time slice is drawn is non-erupting with $\langle \delta z \rangle / x_f < 0.8$ (see Fig. 10) such that the flux rope plasma persists in a quasi-static equilibrium throughout its evolution. In the left panel of Fig. 11, the poloidal magnetic field $\mathbf{B}_P$ is plotted in vectors with the toroidal current J_T in color. In the right panel, the poloidal current density $\mathbf{J}_P$ is plotted in vectors with the plasma toroidal field B_{Ti} in color. At this juncture, we now possess all of the raw quantities that are required to compute the magnetic force density $f(y,z) = \hat{\mathbf{e}}_z \cdot (\mathbf{J} \times \mathbf{B})$. The remaining task is to

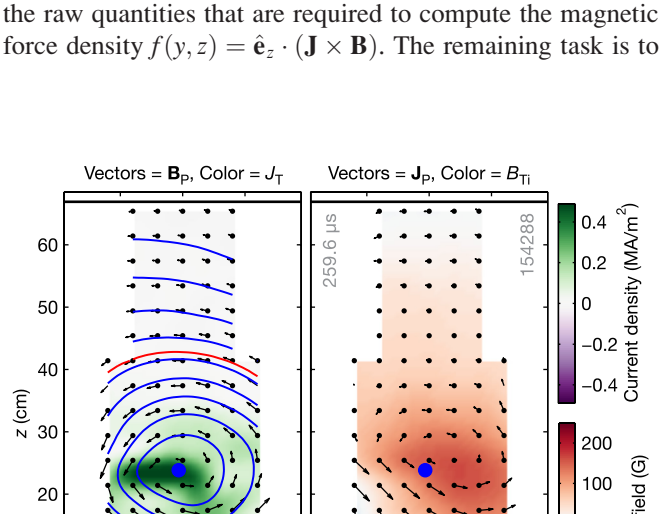

FIG. 11. Magnetic field and current density profiles from a sample non-erupting discharge. On the left is the in-plane poloidal field $\mathbf{B}_P$ and the out-of-plane toroidal current J_T. On the right is the in-plane poloidal current $\mathbf{J}_P$ and the out-of-plane internal toroidal B_{Ti}. The blue contours on the left are contours of the flux function $\psi(y, z)$. The red contour encloses 90% of the toroidal current flowing in the rope and therefore defines the flux rope boundary.

define the minor radius, $a(\theta)$, that sets the in-plane limits on the volumetric integration of the force densities.

In order to define the in-plane boundary of the flux rope, we define a local poloidal flux function $\psi(y, z)$, that is directly related to the toroidal vector potential A_T via $\psi(y,z) = h_T(z)\,A_T(y,z)$. It can be computed by integrating along any integration path $C = C_y + C_z$ as

$$\psi(y,z) = -\int_{C_y} dy\, h_T B_z + \int_{C_z} dz\, h_T B_y. \tag{32}$$

In practice the integration path is chosen to run vertically along the center probe of the array and then left and right at each z value. This ensures that residual integration errors are minimized. The flux function determined from Eq. (32) is only unique if the in-plane poloidal magnetic field measured by the probes is divergence free. Unfortunately, small measurement errors can introduce a non-zero divergence into the measured fields. As such, the in-plane fields are processed using a "divergence cleaning" technique that removes any magnetic field divergence introduced by measurement errors. The procedure for the diverge cleaning technique is described in detail in Appendix B. Sample contours of the integrated flux function as determined from divergence-cleaned fields are shown in blue in the left panel of Fig. 11.

What remains is to use $\psi(y, z)$ to formally define the boundary of the flux rope (i.e., its minor radius). Defining the boundary of the flux rope in the y-z plane is an important task for two reasons: (1) this boundary sets the limits of integration in the force per unit length calculations; and (2) several of the analytical models developed in Section II B rely on the apex minor radius a_{ap} as an input. In this paper, we define the boundary of the flux rope as the poloidal flux contour that encloses 90% of the measured toroidal current. The value of the flux function at this boundary location is $\psi = \psi_{edge}$. In practice, the exact percentage of enclosed current does not substantially modify the force measurement results. The contour that encloses 90% of the toroidal current for the flux rope measurements in Fig. 11 is shown in red.

One important issue that becomes clear from Fig. 11 is that the probe array does not capture the entire cross-section of the flux rope. While there are several options for addressing this shortcoming, we choose here to take the simplest approach of scaling all of the integrated quantities by the ratio of the total current passing through the electrodes to the total current measured within the cross-section of the probe array. This measured current scaling gives a reasonable estimate of how much of the current and other integrated quantities (such as forces) are acting outside of the probe array. For the discharge under consideration, this scale factor does not exceed ~1.3 during the main phase of the discharge.

Before presenting the force balance results, it is instructive to examine how the key parameters at the edge of the flux rope evolve as a function of time. In Fig. 12(a), the apex height evolution of the same discharge from Fig. 11 is shown for reference. In Fig. 12(b), measurements of the minor radius show that, once the equilibrium sets up at its peak height, the apex minor radius a_{ap} is much larger than the footpoint radius. This footpoint-to-apex expansion is a key

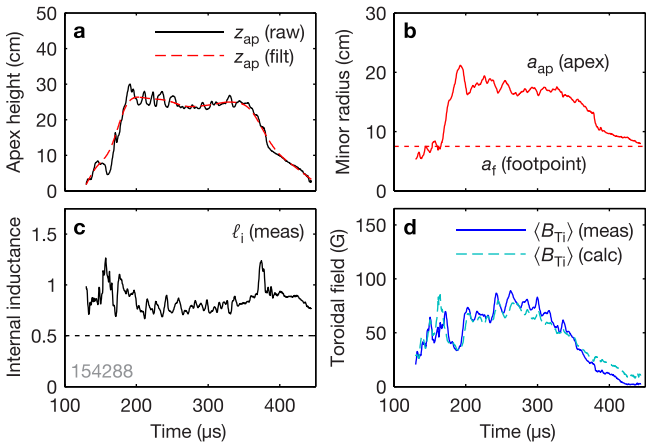

FIG. 12. Time-resolved quantities evaluated at $\psi = \psi_{edge}$ at each time point during the discharge. (a) Apex height evolution $z_{ap}(t)$. (b) Expansion of the apex minor radius a_{ap} during the main phase of the discharge. Note that the aspect ratio is less than 1.5. (c) Measured normalized internal inductance ℓ_i. Values above 0.5 indicate a somewhat peaked current profile. (d) Calculated (via Eq. (26)) and measured average paramagnetic toroidal field in the rope cross-section. Parameters such as z_{ap}, a_{ap}, and ℓ_i are key for evaluating the analytical expressions derived in Section II B.

feature of the low-aspect-ratio, line-tied flux rope. Figure 12(c) shows the measured values of the normalized internal inductance $\ell_i \equiv \langle B_P^2\rangle / B_{Pa}^2$, which hovers just below unity for most of the discharge. Finally, in Fig. 12(d), we see that the measured $\langle B_{Ti}\rangle$ matches well with the analytical expression from Eq. (26) throughout the discharge. This is a strong indication of the effectiveness of the 1D force-free model for the paramagnetic toroidal field that was developed in Section II B 4. The validity of this analytical expression is examined in more detail in Section V. Most importantly, Fig. 12 demonstrates that the methods developed in this section permit the direct measurement of key parameters such as z_{ap}, a_{ap}, and ℓ_i that are required to evaluate the analytical expressions developed in Section II B.

The above analysis techniques provide all of the necessary information to use Eq. (4) to measure the various forces per unit length acting on the flux rope apex. In particular, we can now directly integrate each $\mathbf{J}\times\mathbf{B}$ term in Table II to examine the various contributions to the force-free equilibrium. The results of these laboratory force measurements for two sample discharges are shown in Fig. 13. Here, the experimental measurements are plotted as solid patches of color, while the corresponding analytical models are plotted as solid lines of the same color. The positive and negative forces are added one on top of the other, and the net force, which is the sum of all of the *measured* force terms, is shown in black. All of the forces are normalized to $F_{\text{norm}} \equiv \mu_0 I_T^2/4\pi x_f$. The small value of the net force when compared to the individual force terms indicates that a quasi-force-free equilibrium is, in fact, achieved in these experiments. This is one of the key conclusions of this paper: that a force-free equilibrium is measured by considering only the hoop, strapping, and tension Lorentz force terms. This conclusion, which validates the low-β assumption in these experiments, will be substantiated with a database-wide comparison of measured forces in Section V.

Upon examining the various force terms shown in Fig. 13, we see that, as expected, the hoop force pushes upward while the strapping and toroidal tension forces pull downward. When

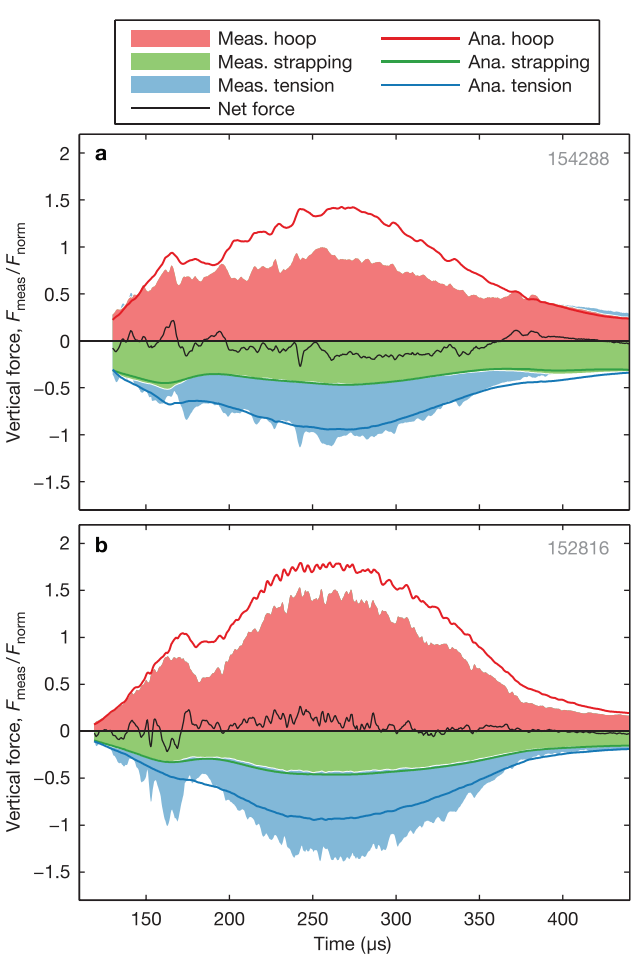

FIG. 13. Two examples of experimentally measured forces at the flux rope apex. The measured forces are represented by the solid colored patches, while their corresponding analytical predictions are represented by the same-colored lines. The net force measured in the experiment is shown in black, indicating that quasi-force-free equilibrium is achieved.

comparing to the analytical expectations, the strapping force is very well predicted in both cases. The hoop force, on the other hand, is weaker in both cases than is predicted analytically. Finally, the toroidal field tension force matches well in one case, but is stronger than predicted in the other. As we show in Section V, these trends continue across a database of several hundred shots: the strapping force is accurately predicted, while the tension and hoop forces are more susceptible to variations in the experimental parameters.

V. DATABASE-WIDE COMPARISON OF LABORATORY AND ANALYTICAL FORCES

In this section, we apply the force measurement techniques developed in Section IV to a database of flux rope plasmas that spans a wide range of experimental conditions. The central goal is to validate the various analytical force models developed in Section II B. The flux rope database considered here is a subset of the ~800 discharge database that is used to analyze the torus vs. kink instability parameter space in Fig. 10. Since the present objective is to quantify the quasi-steady forces acting on each flux rope plasma, only non-erupting discharges with $\langle \delta z\rangle / x_f < 0.8$ are considered. This condition reduces the database by half. The further requirement that the magnetic probe array be aligned in the y-z

plane in order to measure the flux rope forces leaves the final force database with ~200 viable discharges. The non-erupting flux rope plasmas in the force database span three of the four quadrants of the torus vs. kink instability parameter space in Fig. 10 and therefore provide a broad sampling of flux rope parameters.

To analyze the measured and predicted forces across the force database, the various time-resolved force waveforms in Fig. 13 must be reduced to a single value per force term per discharge. This is accomplished here by averaging over the peak 5% of the discharge as defined by the toroidal current injected at the electrodes (see Fig. 9). For the two sample discharges in Fig. 13, this constitutes an average over ~20 μs in the vicinity of $t = 275\ \mu$s. Note that each force waveform is filtered prior to averaging to eliminate transient deviations from the mean.

Figure 14 summarizes the database-wide force analysis. Here, the measured values for each force term are plotted against their corresponding analytical predictions, which are summarized in Table II. The goodness-of-fit between the measured forces and the analytical predictions is quantified here in terms of a residual of the form

$$\text{Res.} \equiv \sqrt{\frac{1}{N}\sum_{j}^{N}\left(\frac{F_{\text{meas},j} - F_{\text{calc},j}}{F_{\text{norm}}}\right)^2}, \tag{33}$$

where the sum is over all values of a given force term and the forces are normalized to $F_{\text{norm}} \equiv \mu_0 I_T^2/4\pi x_f$. The residuals for the hoop, strapping, and tension force terms are listed in the figure legend.

It is clear that the preliminary trends from the time-resolved force analysis in Fig. 13 continue across the broader force analysis database. First, while the measured hoop force correlates positively with the analytical model, it consistently underperforms its prediction. Second, the strapping force is very well predicted by its analytical model. In some sense this is not surprising given that, unlike the hoop and tension forces, the strapping force does not depend on the arched geometry of the flux rope. Finally, the toroidal field tension force also positively correlates with its analytical model, although it often exceeds the analytical prediction in magnitude. The non-ideal trends in the hoop and tension forces will be examined more thoroughly later in this section.

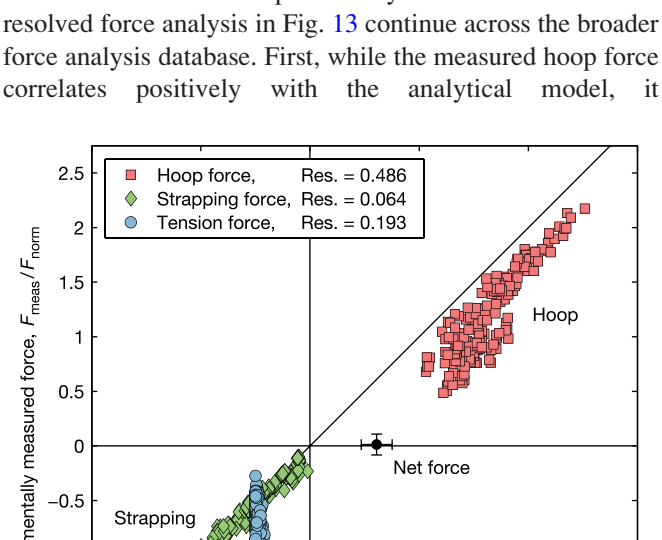

FIG. 14. Measured versus predicted forces across the equilibrium parameter space. The forces are normalized to $F_{\text{norm}} \equiv \mu_0 I_T^2/4\pi x_f$. The strapping force is well-predicted, while the hoop force is consistently weaker than predicted and the tension force is often stronger than predicted. The measured net force is nearly zero, indicating that a force-free equilibrium is measured across the database.

Possibly the most important conclusion from Fig. 14 is that, when all three force terms are summed and averaged over the database, the net force is very nearly zero. To demonstrate this, the mean net force is plotted with error bars as the single black dot in Fig. 14. The fact that the measured net force is zero indicates that a force-free equilibrium is achieved among the hoop, strapping, and tension Lorentz force terms. This validates both the force measurement techniques developed here and the low-β assumption that is applied to these experiments.[18] While the *measured* net force is zero, the *predicted* net force is substantially positive, indicating that the analytical force models expect the equilibrium to be at a higher altitude than is realized in the experiment. This mismatch between the measured and predicted equilibrium heights is expected to have implications for the loss-of-equilibrium/torus instability criterion that are calculated based on these analytical models. Given the length of this manuscript, we defer such analysis to future work.

The database-wide underperformance of the hoop force in Fig. 14 warrants further investigation. In particular, it is instructive to assess the impact of the various line-tying considerations that were introduced in Section II B. As such, Fig. 15 shows the measured hoop forces versus the analytical predictions derived from the four different hoop force models in Fig. 3. In the circular and line-tied image cases (Figs. 15(a) and 15(c)), the higher-magnitude data points diverge substantially to the right, implying that the analytical prediction is too large. These higher magnitude data points correspond to lower-lying ropes, which for the circular case means a small major radius. For the image case, on the other hand, this means a close proximity between the physical loop and its image loop. Both conditions result in large predicted hoop forces that do not match well with the experiment.

The line-tied circle case (Fig. 15(b)) has the opposite problem where the higher-magnitude cases pull to the left. In this case, the low-lying ropes are far from their shifted-circle return loop. Only in the line-tied fixed case do the higher-magnitude points fall in line with the lower-magnitude points. While the residual values of 0.486 do not discern between the line-tied circle and line-tied fixed cases, we conclude based on the slope of the data that the line-tied fixed case, which matches the experimental configuration, performs the best. It is important to note that in each of these cases, induced currents in the stainless steel wall of the vacuum vessel also modify the hoop force. Since the vessel currents oppose the flux rope current, they reduce the measured hoop force. This effect, which is treated in detail in Ref. 17, is included in all four subpanels in Fig. 15 so as not to bias the results.

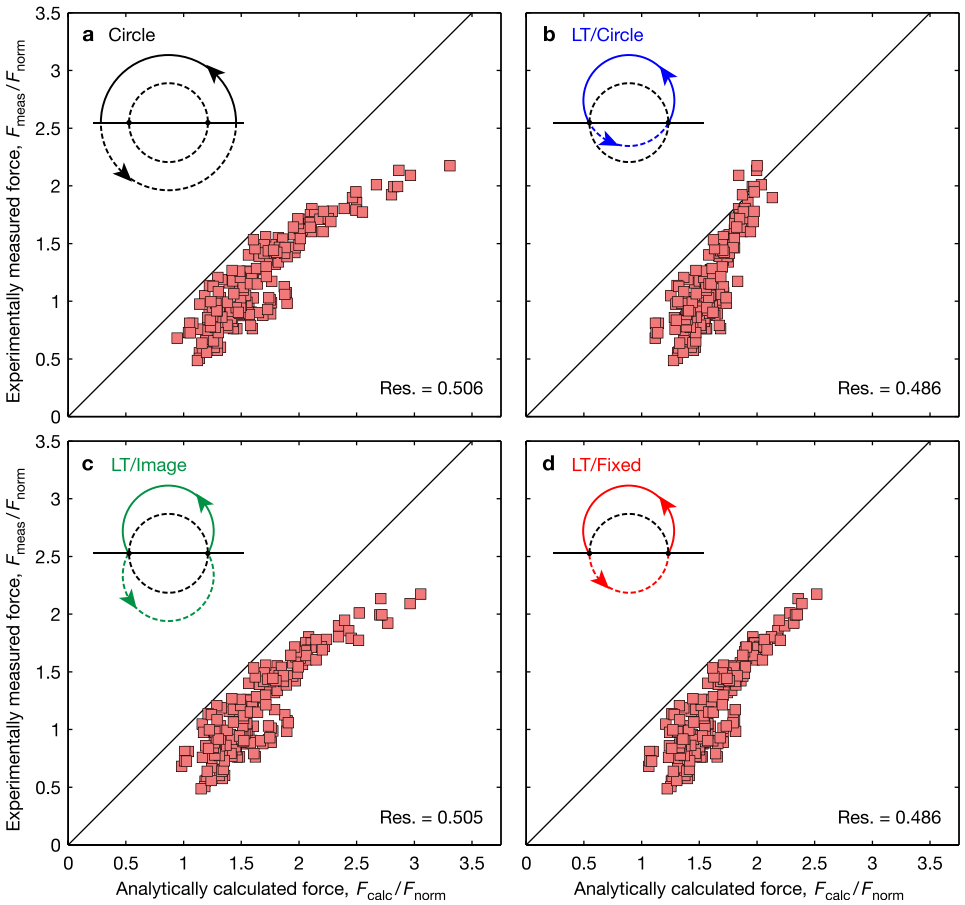

FIG. 15. Comparison of measured versus analytically predicted hoop forces as derived from the four different flux rope models in Fig. 3. The measured data points are the same in each subpanel such that only the predicted data points change. The goodness-of-fit residuals (Eq. (33)) are list in the bottom right of each subpanel. The higher-magnitude cases diverge to the right in (a) and (c) and to the left in (b) due to the different subsurface closures. The line-tied (LT) fixed closure in (d), which most closely matches the experimental configuration, is the case that is used in Fig. 14.

The central conclusions of this extended hoop force analysis are twofold. First, Fig. 15 shows that the line-tied nature of the flux rope and the details of its sub-surface closure are key to accurately predicting the hoop force over a wide range of parameters. Second, even with the line-tied profile and correct sub-surface closure, the hoop force consistently underperforms the analytical prediction. We attribute this latter effect to low-aspect-ratio and line-tying effects that act to rearrange the internal profiles of the flux rope in ways that are not accounted for in the large-aspect-ratio analytical model (Eq. (6)). Given the stringent assumptions of the large-aspect-ratio model, it is not surprising that low-aspect-ratio, line-tied ropes would behave differently than predicted. In fact, it may be more surprising that the median difference between the measured and predicted forces is just 30%.

Given that the strapping force agrees well with its analytical model, we move on to analyze the toroidal field tension force in more detail. The conclusion from Fig. 14 is that the tension force is well-predicted in some cases, but that it can substantially exceed its predicted magnitude in others. It is important to note that the present tension force results should be considered independently of those in Ref. 18. In that case, the focus is on transient enhancements of the tension force that are generated in certain parameter regimes by dynamic magnetic self-organization events. The present analysis, on the other hand, considers only time-averaged, quasi-steady forces in an effort to better understand the flux rope equilibria. As such, the transient tension forces that are the focus of Ref. 18 average out in the present analysis.

The toroidal field tension force derivation in Section II B 4 makes it clear that predicting the cross-section-averaged paramagnetic toroidal field $\langle B_{Ti}\rangle$ is key to predicting the toroidal field tension force (Eq. (20)). According to the analytical expression in Eq. (26), this quantity should depend only on the applied guide field B_{g0} and the edge poloidal field B_{Pa}. Figure 16 compares the experimentally measured paramagnetic field to the analytical prediction from Eq. (26). The figure shows that, in spite of the wide variation in the

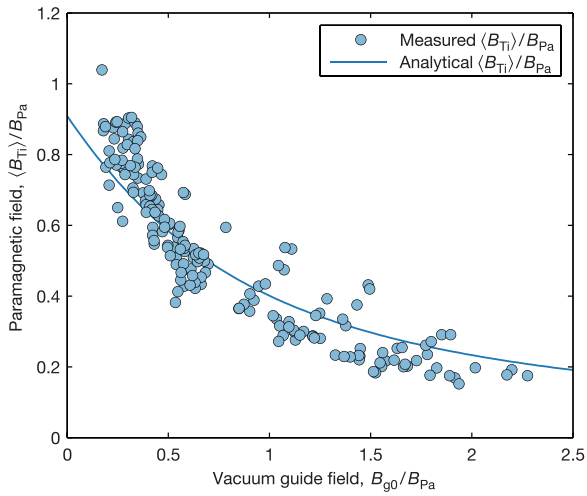

FIG. 16. Comparison of measured $\langle B_{Ti}\rangle$ values with the analytical prediction from Eq. (26). The measured values each represent a single discharge from the force analysis database in Fig. 14. Though there is some scatter in the data, the analytical prediction from Eq. (26) holds quite well across the parameter space.

experimental parameters, the paramagnetic field is quite well predicted analytically. It is impressive that the analytical expression performs so well given that it is derived from a simple 1D model of a linear screw pinch. The good agreement between the experimental measurements and the analytical prediction further confirms that these flux rope plasmas are low-β.

A final conclusion regarding the tension force is that, as can be seen in Fig. 14, the tension force is a substantial contributor to the flux rope equilibrium force balance. Its measured strength in many cases is commensurate with the measured strength of the strapping force. This conclusion is important given that the tension force is often ignored in the analytical treatment of solar flux ropes. One example is the traditional torus instability derivation, which considers only hoop and strapping forces.[10,15] As a final note, the tension force measurements reported in this paper include both magnetic tension and magnetic pressure contributions. While the tension term generally dominates, the pressure term can be non-negligible. This distinction is analyzed further in Appendix C.

VI. SUMMARY AND DISCUSSION

In this paper, the quasi-steady equilibrium forces acting on low-aspect-ratio, line-tied magnetic flux ropes are studied in detail using a well-diagnosed laboratory flux rope experiment. The goal of this study is to inform loss-of-equilibrium solar eruption models that rely on an understanding of such forces to analyze and predict flux rope eruptions in the Sun's corona. Three flux rope force terms are considered in detail: the hoop, strapping, and tension forces. First, analytical models are developed for each force term in Section II and the experimental setup is described in Section III. Then, in Section IV, a laboratory force measurement procedure is developed based on spatially resolved magnetic measurements from within the flux rope plasma. Using this force measurement procedure, we find that a force-free equilibrium is measured across a flux rope database of nearly 200 discharges (Section V). This finding provides two key conclusions: (1) it validates the laboratory force measurement procedure, which is used extensively here and in Ref. 18; and (2) it validates the low-β assumption that is applied to these experiments given that a force-free equilibrium is measured among three purely magnetic force terms.

With the force measurements in hand, we performed detailed comparisons of the various measured force terms to their corresponding analytical predictions. This leads to several conclusions about line-tied flux rope equilibria:

1. While the hoop force does act to drive the flux rope upward, its magnitude is systematically smaller than predicted, even after correcting for the partial toroidal shape of the line-tied rope. This difference is attributed to low-aspect-ratio and line-tying effects not accounted for in the traditional large-aspect ratio analytical models.
2. Assessing the hoop force requires a proper accounting of the partial toroidal shape of the line-tied rope and of the shape of the return path beneath the flux rope footpoints.
3. The strapping force, on the other hand, behaves as expected, increasing with the product of plasma current and strapping field.
4. The toroidal field tension force contributes substantially to the laboratory flux rope equilibra. It can often be larger in magnitude than is predicted analytically. This observation is also attributed to low-aspect-ratio and line-tying effects, but further analysis, likely computational, is required to understand the relative impact of these effects.

We emphasize once again that the toroidal field tension forces studied in this paper are quasi-static forces that contribute to the flux rope equilibrium force balance. These quasi-static forces differ fundamentally from the dynamic tension forces that are reported in Ref. 18. An exploration of the relationship between these two tension forces is left for future work.

The conclusions of this paper represent an enhanced understanding of the Lorentz forces that act on line-tied flux ropes. In particular, the combination of a weaker-than-expected hoop force and stronger-than-expected toroidal field tension force results in lower altitude flux rope equilibria than are predicted analytically. This deviation from the analytical predictions is expected to impact the expected loss-of-equilibrium criteria for analogous flux ropes in the solar corona.

Several opportunities remain for further analysis of the laboratory data. In particular, the observed $n \sim 0.8$ torus instability criterion is quite intriguing. With the enhanced understanding of the equilibrium forces provided by this paper, this reduced loss-of-equilibrium threshold should be investigated in the context of the partial torus instability of Olmedo and Zhang.[19] Experimental factors such as the series inductance of the capacitor bank are expected to contribute to this reduced instability criterion, but the effects of line-tying are fundamental to both the laboratory experiments and the solar corona. The impact on the hoop force as shown in Fig. 4 should be considered. Furthermore, the question of how much of the reduced threshold is due to low aspect ratio and line-tying effects should be explored. This may ultimately help to pin down the torus instability threshold in line-tied systems.

The differences between the analytical predictions and laboratory measurements presented in this paper highlight the need to further understand how idealized analytical predictions are modified in the highly three-dimensional, line-tied conditions of the solar corona. In our view, computational analysis of the laboratory flux ropes studied here and of analogous systems in the solar corona represents the best chance to strengthen the connection between our laboratory results and observations of solar flux ropes. At a minimum, the results presented in this paper pose several sharp questions that can serve as a launching point for a numerical simulation effort: Can the same equilibrium effects of a weakened hoop force and a heightened tension force be recovered numerically? Are these effects a consequence of low aspect ratio and/or line-tying as we postulate here? How do these considerations modify the expected loss-of-equilibrium criterion? Answering such questions, and determining how these results can be applied to flux ropes in the Sun's corona, is an important step on the path toward understanding and ultimately predicting solar eruptive events.

ACKNOWLEDGMENTS

The authors thank R. Cutler, E. E. Lawrence, F. Scotti, P. Sloboda, E. Oz, and T. D. Tharp for technical contributions and R. M. Kulsrud for useful discussions. This research is supported by Department of Energy (DoE) Contract No. DE-AC02-09CH11466 and by the National Science Foundation/DoE Center for Magnetic Self-Organization (CMSO). The digital data for this paper can be found at http://arks.princeton.edu/ark:/88435/dsp014x51hm50z.

APPENDIX A: FLUX ROPE TOROIDAL CURVATURE MEASUREMENTS

As described in Section IV, the direct measurement of the magnetohydrodynamic forces at the apex of the flux rope requires a measurement of the out-of-plane (toroidal) curvature κ_T. Due to the line-tied nature of the flux ropes studied here, κ_T is, in general, a non-trivial function of z. From vector calculus arguments,[20] $\kappa_T(z)$ is related to the curvilinear scale factor $h_T(z)$ via

$$\kappa_T \equiv \frac{1}{R_c} = \frac{1}{h_T}\frac{\partial h_T}{\partial z}, \tag{A1}$$

where R_c is the toroidal radius-of-curvature. This equation can be inverted to get

$$h_T = \exp\left\{\int dz\, \kappa_T(z) + C_0\right\}, \tag{A2}$$

where the integration constant C_0 is chosen so that $h_T(z_{ap}) = R_c(z_{ap})$. This ensures that the coordinate T represents the angular toroidal displacement along the magnetic axis of the flux rope. From the above relationship, we see that a measurement of $\kappa_T(z)$ is required in order to compute $h_T(z)$ and carry out the force balance analysis. We now demonstrate the procedure for measuring $\kappa_T(z)$ in the MRX flux rope discharges.

The MRX force measurements can only be carried out in flux rope discharges where the magnetic probe is array aligned in the y-z (poloidal) cross-section of the flux rope (see Fig. 7). This is because the integrals over r and θ in Eq. (4) require full poloidal resolution. As we will see, however, measuring the toroidal curvature requires that the probes be aligned instead in the x-z (toroidal) cross-section. Thus, the force measurement procedure developed here uses a multi-discharge approach where curvature measurements from x-z-aligned discharges are used to evaluate the forces in y-z-aligned discharges.

The general expression for the curvature of a magnetic field line is given by

$$\boldsymbol{\kappa} = (\mathbf{b}\cdot\nabla)\,\mathbf{b}, \tag{A3}$$

where $\mathbf{b} \equiv \mathbf{B}/B$ is the magnetic field unit vector. In Cartesian (x, y, z) coordinates, this expression expands to nine terms (three for each of the three vector components). Here, we are interested in the z-directed (vertical) curvature, which is given by

$$\hat{\mathbf{e}}_z \cdot (\mathbf{b}\cdot\nabla)\,\mathbf{b} = b_x\frac{\partial b_z}{\partial x} + b_y\frac{\partial b_z}{\partial y} + b_z\frac{\partial b_z}{\partial z}. \tag{A4}$$

As we will see, $b_z\partial_z b_z$ is small when evaluated at the flux rope apex (on the z axis). This leaves the first two terms as the dominant components of the vertical curvature.

To demonstrate the evaluation of Eq. (A4), we examine magnetic probe data from two nearly identical stable discharges, one with the probe array in the x-z plane and the other with the probe array in the y-z plane (see Fig. 17). These magnetic field data are the vector measurements $\mathbf{B}(0, 0, z)$ acquired along the z-axis by the central probe in the magnetic probe array. The specific measurements in Fig. 17(a) are taken from the two discharges shown in Fig. 7. Here, B_x is the local toroidal field $(B_g + B_{Ti})$, while B_y is the local poloidal field $(B_s + B_{Pi})$. The agreement between the data from the two discharges is excellent, thereby confirming their similarity. It should be noted, however, that the z locations of the plasma fields in the x-z discharge were scaled by $\sim$1.1 in order to match the height of the flux rope in the y-z discharge.

With the magnetic field data in hand, we now evaluate the various curvature terms in Eq. (A4). The evaluation is carried out about the center probe in the array with the numerical derivative data being sourced from the probes to the left and right of the center probe. The results for the discharges under consideration are shown in Fig. 17(b). The $b_x\partial_x b_z$ term comes from the x-z discharge, the $b_y\partial_y b_z$ term from the y-z discharge, and the $b_z\partial_z b_z$ term from both discharges. As expected, this final term is small compared to the other two. We see that the remaining terms represent the major radius (toroidal) curvature and the minor radius (poloidal) curvature, respectively. Since we are interested in the major radius curvature, we focus on the $b_x\partial_x b_z$ term and define

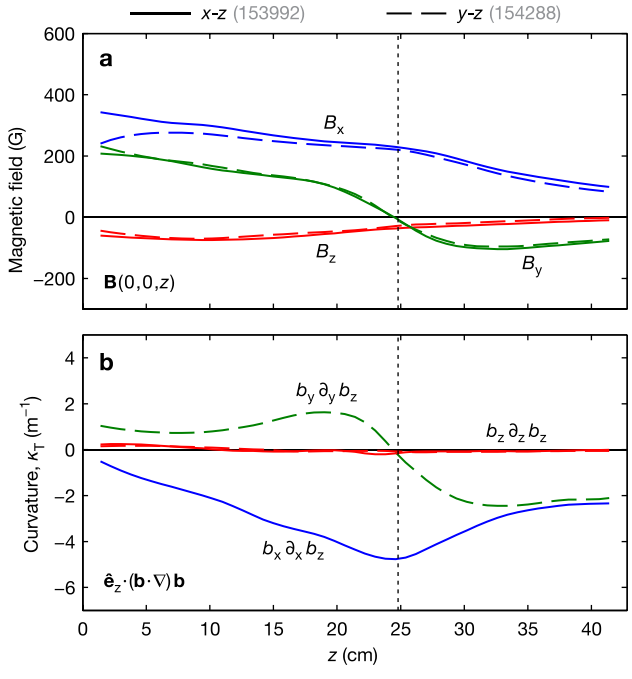

FIG. 17. Experimentally measured terms of the vertical flux rope curvature (Eq. (A4)). Solid lines are from the x-z probe alignment, while dashed lines are from the y-z probe alignment. Note that the dominant vertical curvature components in the right panel are the toroidal curvature (blue) and poloidal curvature (dashed green).

$$\kappa_T \equiv -b_x \frac{\partial b_z}{\partial x}. \tag{A5}$$

Thus, the toroidal curvature profile $\kappa_T(z)$ can be directly measured from probe data acquired in the x-z plane and used in the analysis of data acquired in the y-z plane.

The curvature analysis procedure developed here can now be applied to the range of x-z-aligned discharges in the MRX flux rope database. Of the 800+ shots in the database, only ~200 of them were acquired with the probe array in the x-z configuration. Furthermore, only half of the 200 x-z-aligned discharges are "non-erupting" as established by the $\langle \delta z \rangle / x_f < 0.8$ definition used throughout this paper (see Sections III D and V). This leaves a set of ~100 x-z-aligned discharges from which to develop an understanding of the toroidal curvature of the laboratory flux ropes.

Ideally, each y-z-aligned discharge would have a corresponding x-z aligned discharge from which to extract curvature information. In practice, not enough data is available to facilitate this one-to-one mapping. Instead, the simplest approach with the available x-z aligned discharges is to aggregate the curvature measurements from all available discharges to generate ensemble-averaged curvature and curvilinear scale factor profiles. To do this, the curvature profiles for each discharge are first averaged over 150 μs in the middle of the discharge. Then, all of the time-averaged profiles are combined via a weighted average to produce the ensemble-averaged curvature profiles shown in Fig. 18.

In Fig. 18(a), the ensemble-averaged curvature profile is shown along with a model "line-tied" curvature profile derived from the shifted-circle flux rope model described by Eq. (9). The aggregate apex height of the flux rope is also shown. Fig. 18(b) shows the normalized curvilinear scale factor $\hat{h}_T \equiv h_T / R_c(z_{ap})$ that results from applying Eq. (A2) to the measured curvature profile in Fig. 18(a). The measured scale factor profile shows that the actual apex wedge integration volume is notably wider underneath the rope ($z < z_{ap}$) and narrower above the rope ($z > z_{ap}$) than is predicted by the line-tied model.

A final wrinkle is that a subset of the discharges used in the flux rope force study in Sections IV and V are not well-described by the aggregate curvature profile in Fig. 18. This is because these discharges were taken with a smaller footpoint separation distance ($x_f = 15$ cm versus $x_f = 18$ cm) than all of the discharges that contribute to Fig. 18. Unfortunately, no x-z discharges were taken in the $x_f = 15$ cm configuration. As such, the line-tied curvature model is used as the curvature profile for the $x_f = 15$ cm discharges.

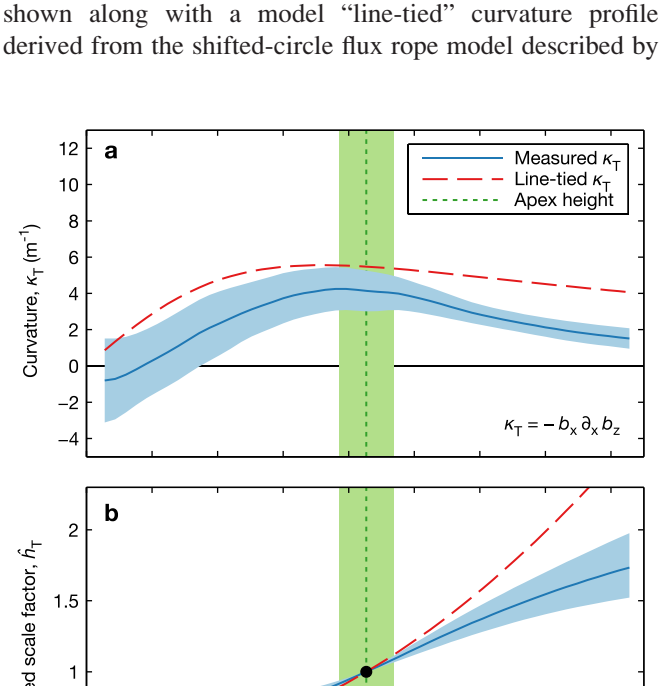

FIG. 18. Aggregate experimentally measured toroidal curvature and scale factor profiles for the MRX flux rope database. On average, the measured h_T profile makes for a wider integration volume under the rope and a narrower volume above the rope when compared to the shifted-circle.

APPENDIX B: DIVERGENCE CLEANING OF THE IN-PLANE MAGNETIC FIELD DATA

A crucial aspect of the force analysis presented in this paper is the ability to define a local poloidal flux function (see Eq. (32)). In order for the flux function to be unique, however, the measured magnetic fields must be divergence free ($\nabla \cdot \mathbf{B} = 0$). This can become a problem when experimental noise and measurement errors inject residual divergence into the measurements. Fortunately, we can take advantage of the assumed local toroidal symmetry of the flux rope to implement a "divergence cleaning" procedure that removes any residual divergence from the in-plane components of the y-z magnetic field data. In particular, given the toroidal scale factor h_T (see above) and the assumption that $\partial/\partial T \simeq 0$, the divergence of the magnetic field is given by

$$\nabla \cdot \mathbf{B} = \frac{\partial B_y}{\partial y} + \frac{1}{h_T} \frac{\partial (h_T B_z)}{\partial z}, \tag{B1}$$

which depends only on the in-plane field components B_y and B_z and their in-plane derivatives. The divergence cleaning procedure implemented here uses an iterative technique to diffuse away the divergence[47]

$$\mathbf{B}^{n+1} = \mathbf{B}^n + (\delta r)^2 \nabla [\nabla \cdot \mathbf{B}^n], \tag{B2}$$

$$\mathbf{B}^N = \mathbf{B}^0 + (\delta r)^2 \sum_{n=0}^{N-1} \nabla [\nabla \cdot \mathbf{B}^n], \tag{B3}$$

where n is the iteration index and δr is a characteristic diffusion length scale. The convergence of the iteration is faster for larger δr, but numerical stability ultimately limits its magnitude. An interesting feature of this divergence cleaning method is that the resulting field $\mathbf{B}^N$ will give the exact same toroidal current density as the initial field $\mathbf{B}^0$. This is because $\mathbf{J} = \nabla \times \mathbf{B}/\mu_0$ and $\nabla \times \nabla g = 0$ for all scalar functions g. Thus, since the added divergence cleaning terms are all gradients of a scalar, they do not modify the measured current density. Simply stated, this technique finds the in-plane magnetic field that is both divergence free and corresponds to the originally measured toroidal current density.

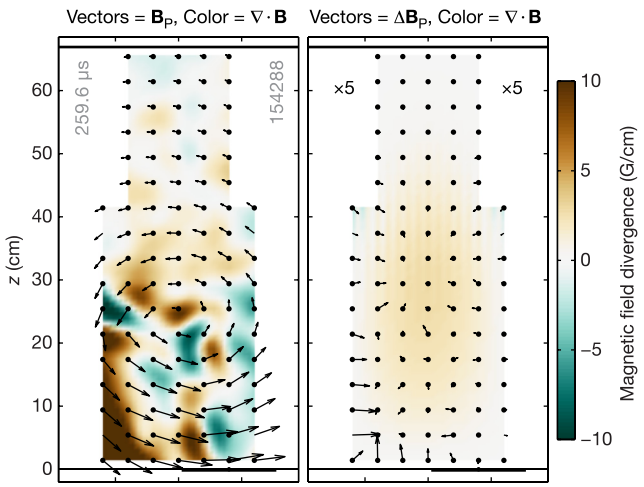

FIG. 19. Sample results from the divergence cleaning of in-plane magnetic field data. Left: Raw poloidal field vectors and their divergence (color). Right: Difference between the raw and cleaned poloidal field data (vectors) and the divergence of the cleaned data (color). Both quantities on the right are amplified by a factor of five (×5).

In practice, the divergence cleaning technique implemented here is very effective, if somewhat computationally intensive. Each time point requires tens of iterations to converge, but the results are excellent (see Fig. 19). In the left panel of this figure, the vectors show the raw poloidal magnetic field measurements $\mathbf{B}_P$ while the colors show their computed divergence. In the right panel, the vectors instead show the difference between the raw and cleaned data $\Delta\mathbf{B}_P$ while the color shows the divergence of the cleaned fields. Note that both the vectors and the colors in the right panel are amplified by a factor of five (×5) in order to appear as something other than zero. The plots show that the divergence is reduced by at least an order of magnitude and that the overall modification to the interpolated magnetic field data is less than 10%. In fact, for the case shown, the average change in the field magnitude is $\langle|\Delta\mathbf{B}_P|/|\mathbf{B}_P|\rangle \sim 7\%$.

APPENDIX C: ADDITIONAL TENSION FORCE ANALYSIS

A remaining concern with the tension force analysis in Section V is how to reconcile the good agreement between the measured and predicted paramagnetic toroidal field in Fig. 16 with the modest agreement between the measured and predicted toroidal field tension force in Fig. 14. Recall from Section II B 4 that two related analytical models were developed for the tension force: Eqs. (20) and (27). The latter expression is used as the analytical tension force model in Fig. 14 since it is this model that is assumed in the canonical torus instability derivations.[10,15] In order to understand the comparison between the two tension force models, however, we now plot the measured tension force data against each of the two models (see Figs. 20(a) and 20(b), respectively). The stiffness of Eq. (27), which assumes that $\langle B_T^2\rangle - B_{g0}^2 \simeq B_{Pa}^2$, is evident in Fig. 20(a). More scatter is observed in Fig. 20(b), on the other hand, which uses the experimentally measured values of $\langle B_T^2\rangle - B_{g0}^2$. Based on the residuals, it is not clear that either of the models captures the tension force behavior.

Further insight can be gained by recognizing that the source term for the toroidal field tension force, $f_t = -J_P B_T$, is actually comprised of a magnetic tension term and a magnetic pressure term

$$f_{Tt} = -\left(\frac{B_{Ti}}{\mu_0 R}\right)B_T, \tag{C1}$$

$$f_{Tp} = -\left(\frac{1}{\mu_0}\frac{\partial B_{Ti}}{\partial R}\right)B_T. \tag{C2}$$

The contributions from each of these two terms are explicitly separated in Fig. 20(c). In this case, the tension term shows much better agreement with the model. The pressure term can be negligible in some cases but important in others. It turns out that the cases where the magnetic pressure term is large are those that around low-lying and bound closely to the surface. We again postulate that these effects are

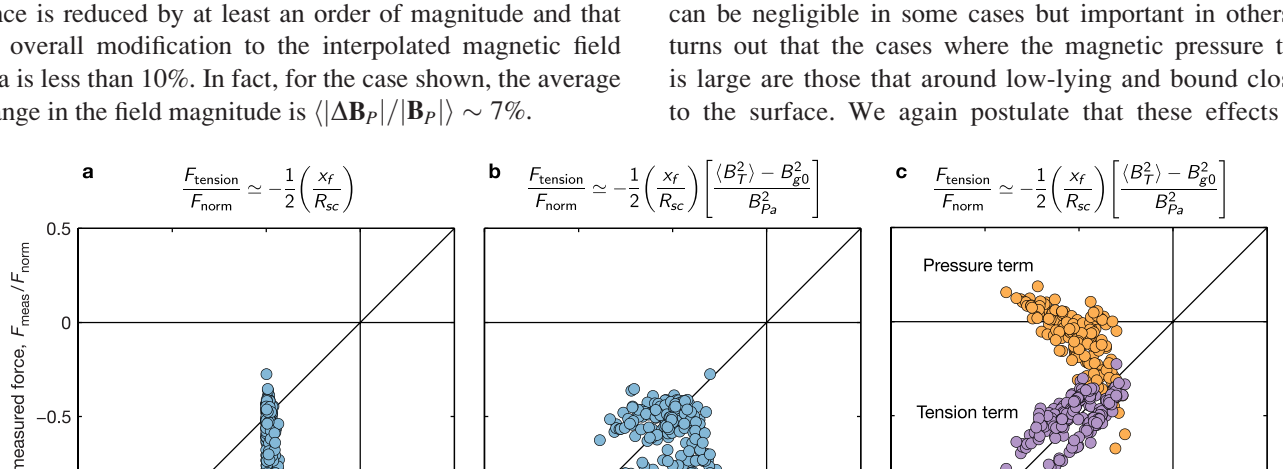

FIG. 20. Comparison of measured data to various analytical tension force models. (a) Comparison to Eq. (27), which is the model that is used in Fig. 14 and in the traditional torus instability derivation. (b) Comparison to Eq. (20), which uses the measured values of $\langle B_T^2\rangle - B_{g0}^2$. (c) Decomposition of the results in (b) into toroidal field tension and pressure terms. The agreement with the tension term is very good. The pressure term is negligible in some cases, but can be important in others.

due to a reconfiguration of the internal flux rope profiles due to low-aspect-ratio and line-tying effects that are not captured by the simplistic analytical models developed in Section II B. Further analysis, likely computational, is required to better understand the relationship between the toroidal field tension and pressure terms in various flux rope equilibria.

[1]*Coronal Mass Ejections*, edited by H. Kunow, N. U. Crooker, J. A. Linker, R. Schwenn, and R. von Steiger (Springer, 2006), Chap. 2, 12.
[2]T. Amari, A. Canou, and J.-J. Aly, Nature **514**, 465 (2014).
[3]M. Kuperus and M. A. Raadu, Astron. Astrophys. **31**, 189 (1974).
[4]J. Chen, Astrophys. J. **338**, 453 (1989); see http://adsabs.harvard.edu/abs/1974A&A....31..189K.
[5]V. S. Titov and P. Démoulin, Astron. Astrophys. **351**, 707 (1999); see http://adsabs.harvard.edu/abs/1999A%26A...351..707T.
[6]I. I. Roussev, T. G. Forbes, T. Gombosi, I. Sokolov, D. De Zeeuw, and J. Birn, Astrophys. J. Lett. **588**, L45 (2003).
[7]T. Forbes, J. Linker, J. Chen, C. Cid, J. Kóta, M. Lee, G. Mann, Z. Mikić, M. Potgieter, J. Schmidt, G. Siscoe, R. Vainio, S. Antiochos, and P. Riley, Space Sci. Rev. **123**, 251 (2006).
[8]L. M. Green and B. Kliem, Astrophys. J. Lett. **700**, L83 (2009).
[9]T. G. Forbes and P. A. Isenberg, Astrophys. J. **373**, 294 (1991).
[10]B. Kliem and T. Török, Phys. Rev. Lett. **96**, 255002 (2006).
[11]Y. Fan and S. E. Gibson, Astrophys. J. **668**, 1232 (2007).
[12]Y. Liu, Astrophys. J. Lett. **679**, L151 (2008).
[13]P. Démoulin and G. Aulanier, Astrophys. J. **718**, 1388 (2010).
[14]A. Savcheva, E. Pariat, A. van Ballegooijen, G. Aulanier, and E. DeLuca, Astrophys. J. **750**, 15 (2012).
[15]G. Bateman, *MHD Instabilities* (MIT Press, 1978).
[16]G. Gary, Sol. Phys. **203**, 71 (2001).
[17]C. E. Myers, "Laboratory study of the equilibrium and eruption of line-tied magnetic flux ropes in the solar corona," Ph.D. thesis (Princeton University, 2015).
[18]C. E. Myers, M. Yamada, H. Ji, J. Yoo, W. Fox, J. Jara-Almonte, A. Savcheva, and E. E. DeLuca, Nature **528**, 526 (2015).
[19]O. Olmedo and J. Zhang, Astrophys. J. **718**, 433 (2010).
[20]B. R. Kusse and E. A. Westwig, *Mathematical Physics: Applied Mathematics for Scientists and Engineers* (Wiley-VCH, 2006).
[21]V. Shafranov, in *Reviews of Plasma Physics*, edited by M. A. Leontovich (Consultants Bureau Enterprises, 1966), Vol. 2, pp. 103–152.
[22]J. D. Jackson, *Classical Electrodynamics* (Wiley, 1999).
[23]J. Wesson, *Tokamaks* (Clarendon Press, Oxford, 1987).
[24]K. Miyamoto, *Plasma Physics and Controlled Nuclear Fusion* (Springer, New York, 2005).
[25]P. A. Isenberg and T. G. Forbes, Astrophys. J. **670**, 1453 (2007).
[26]T. Török and B. Kliem, Astron. Nachr. **328**, 743 (2007).
[27]B. Kliem, J. Lin, T. G. Forbes, E. R. Priest, and T. Török, Astrophys. J. **789**, 46 (2014).
[28]M. Kruskal and M. Schwarzschild, Proc. R. Soc. London A **223**, 348 (1954).
[29]V. Shafranov, Sov. J. At. Energy **1**, 709 (1956).
[30]T. Gold and F. Hoyle, Mon. Not. R. Astron. Soc. **120**, 89 (1960).
[31]T. Sakurai, Publ. Astron. Soc. Jpn. **28**, 177 (1976); see http://adsabs.harvard.edu/abs/1976PASJ...28..177S.
[32]A. W. Hood and E. R. Priest, Geophys. Astrophys. Fluid Dyn. **17**, 297 (1981).
[33]Z. Mikić, D. D. Schnack, and G. van Hoven, Astrophys. J. **361**, 690 (1990).
[34]Y. Fan and S. E. Gibson, Astrophys. J. **609**, 1123 (2004).
[35]T. Török, B. Kliem, and V. S. Titov, Astron. Astrophys. **413**, L27 (2004).
[36]T. Török and B. Kliem, Astrophys. J. **630**, L97 (2005).
[37]S. Inoue and K. Kusano, Astrophys. J. **645**, 742 (2006).
[38]J. P. Freidberg, *Ideal Magnetohydrodynamics* (Plenum Press, 1987).
[39]S. C. Hsu and P. M. Bellan, Phys. Rev. Lett. **90**, 215002 (2003).
[40]I. Furno, T. P. Intrator, D. D. Ryutov, S. Abbate, T. Madziwa-Nussinov, A. Light, L. Dorf, and G. Lapenta, Phys. Rev. Lett. **97**, 015002 (2006).
[41]W. F. Bergerson, C. B. Forest, G. Fiksel, D. A. Hannum, R. Kendrick, J. S. Sarff, and S. Stambler, Phys. Rev. Lett. **96**, 015004 (2006).
[42]E. Oz, C. E. Myers, M. Yamada, H. Ji, R. M. Kulsrud, and J. Xie, Phys. Plasmas **18**, 102107 (2011).
[43]M. Yamada, H. Ji, S. Hsu, T. Carter, R. Kulsrud, N. Bretz, F. Jobes, Y. Ono, and F. Perkins, Phys. Plasmas **4**, 1936 (1997).
[44]J. F. Hansen and P. M. Bellan, Astrophys. J. **563**, L183 (2001).
[45]H. Soltwisch, P. Kempkes, F. Mackel, H. Stein, J. Tenfelde, L. Arnold, J. Dreher, and R. Grauer, Plasma Phys. Controlled Fusion **52**, 124030 (2010).
[46]S. K. P. Tripathi and W. Gekelman, Phys. Rev. Lett. **105**, 075005 (2010).
[47]B. Marder, J. Comput. Phys. **68**, 48 (1987).
[48]J. Chen and J. Krall, J. Geophys. Res. Space **108**, 1410, doi:10.1029/2003JA009849 (2003).